Experimental Mechanics manuscript No.
(will be inserted by the editor)

Y-Shaped Cutting for the Systematic Characterization of Cutting and Tearing

B. Zhang · C.-S. Shiang · S.J. Yang · S.B. Hutchens

Received: September 11, 2018 / Accepted: January 21, 2019

This is a post-peer-review, pre-copyedit version of an article published in Experimental Mechanics. The final authenticated version is available online at: http://dx.doi.org/10.1007/s11340-019-00476-5

Abstract Though they share the similarity of inducing material failure at a crack tip, the cutting and tearing energies of soft materials cannot be quantitatively related to one another. One of the reasons for this lack of understanding comes from additional complications that arise during standard cutting techniques. Decades ago, Lake and Yeoh [Int. J. of Fracture, 1978] described a natural rubber cutting method that uses a 'Y-shaped' sample geometry to mitigate several of these challenges, including minimizing friction and controlling the strain energy available to drive fracture. The latter, understood via a fracture mechanics framework, enables relative tuning between a tearing contribution to the cutting energy and a cutting contribution. In this

B. Zhang, C.-S. Shiang, and S.J. Yang
University of Illinois at Urbana-Champaign

S.B. Hutchens
University of Illinois at Urbana-Champaign
144 Mechanical Engineering Building, MC-244
1206 W. Green St.
Urbana, IL 61801
E-mail: hutchs@illinois.edu

manuscript, we extend Lake and Yeoh's largely unreplicated results to softer, more highly deformable polydimethylsiloxane (PDMS) materials. The range of applicability of this technique to variations in material response, sample geometry, boundary conditions, and cutting rate is large. We utilize this flexibility to describe factors leading to the onset of a material-dependent, stick-slip cutting response, which occurs at low cutting rates and high tearing contributions. Furthermore, variation in cutting blade radius reveals a minimum cutting energy threshold even for blades with radii on the order of a few tens of nanometers. For blunter blades, cutting energy reflects the effects of material strain-stiffening. These results establish the Y-shaped cutting geometry as a useful tool in the study of soft fracture.

Keywords Cutting · Tearing · Soft fracture · Rate dependence · Silicone

1 Introduction

Teeth, blades, claws, and needles frequently cut through soft materials and tissues. It is not surprising then that cutting to machine [1], as a surgical technique [2, 3], to capture prey [4], or as a method of failure characterization [5–11] are all extensively described in the literature. In spite of this wealth of information, researchers lack a quantitative relation between the energy required to cut a soft material and the energy required to tear a soft material. Though individual studies demonstrate a cutting technique's sensitivity to changes in material properties [5, 6, 12, 13], findings lack generalizability. An incomplete understanding of the fundamental physical quantities governing cutting failure in soft materials (blade geometry, material response, fracture energy, contact mechanics) hinders quantitative cross-study comparison. Thus, the literature on cutting is fragmented and challenging to unify.

The technique we apply in this manuscript, a 'Y-shaped' sample (Figure 1(b)) in which material displaces past the blade without significant contact, was originally introduced by Lake and Yeoh [14] in the late 70's. This cutting test method possesses

five important features that make it a promising tool to address the gap in understanding between cutting versus tearing types of soft failure.

1. The Y-shaped geometry eliminates (or significantly reduces depending on the material and blade geometry) frictional contributions to the measured cutting energy.
2. Blade geometry may be readily varied with the same ease as other cutting methods.
3. Failure occurs at a controlled rate, a key consideration for time-dependent soft materials.
4. Small variations in loading geometry allow for independently-tunable cutting and tearing energy contributions. This separation of contributions may enable measurement of a quantifiable relationship between the two.
5. A simple expression captures the cutting energy for a wide range of sample and loading geometries, as we verify in this manuscript.

In spite of these features, the technique has yet to find broad application, with the only other known use by Alan Gent in the mid 90's to probe viscoelastic contributions to rubber tearing [15] and examine cutting of much stiffer polyethylene [16]. Lake and Yeoh found that the energy to cut the natural and butadiene rubbers they tested were several times larger than the threshold tearing energy for those materials. Seemingly in contrast, the styrene-butadiene copolymer rubber tested by Gent et al. exhibited a lower energy to cut versus energy to tear at all but the lowest rates tested (where the trend reversed). These results emphasize the importance of constant rate failure tests for time-dependent materials, as only the lowest rates tested by Gent et al. approach the quasi-static threshold tearing energy Lake and Yeoh used for comparison with cutting [15]. Thus, both authors agree that cutting rubbers is more energetically demanding than tearing (at low rates, for the standard commercial blades available at the time). That cutting is "harder" than tearing is often in contrast to common percep-

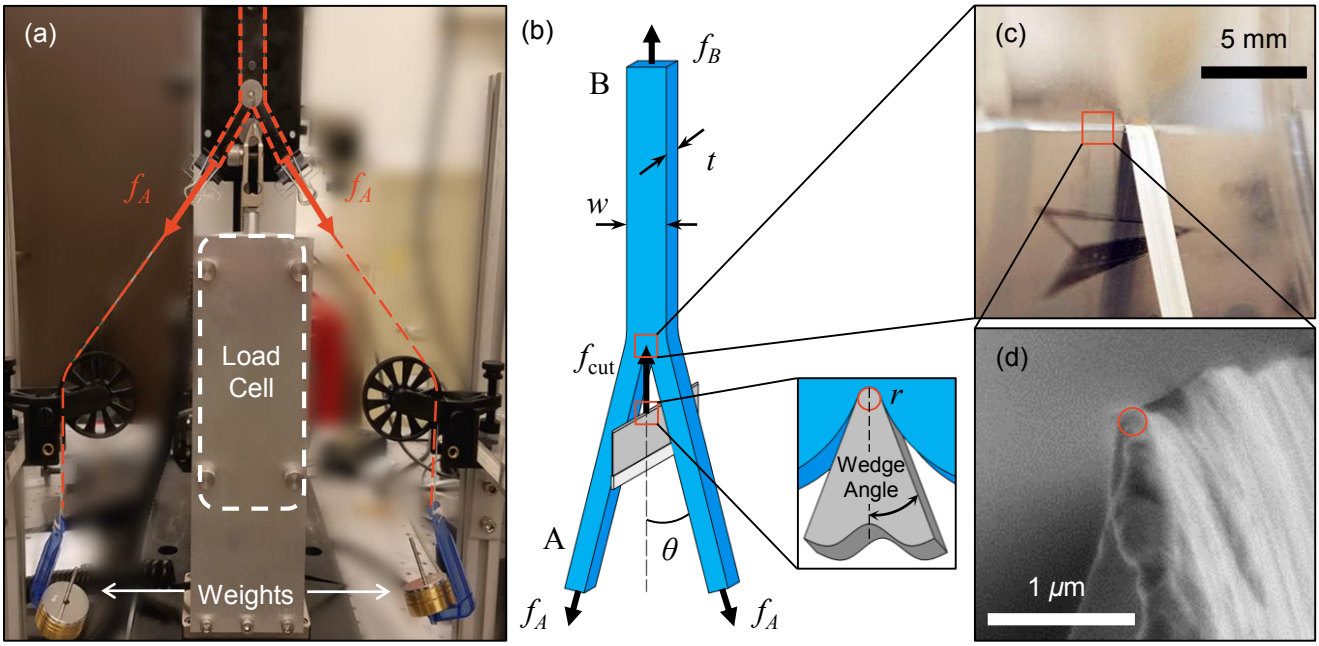

Fig. 1 Cutting with a Y-shaped geometry. (a) A photograph of the cutting instrument shows the position of the sample (orange dashed lines), relative to the load cell (white dashed lines) upon which the cutting blade is mounted. Hanging weights apply load f_A to two sample legs. (b) Schematics of the Y-shaped sample and blade geometries illustrate variable parameters and the free-body diagram during steady-state cutting. The cutting force applied by the blade (c) is measured by the load cell. Blade radius, r, (b)-inset is determined from a scanning electron microscopy (SEM) image (d).

tion and what researchers have measured in other materials, e.g., paper [17], likely due to the primary challenges facing soft cutting and soft failure more generally.

We categorize three types of complications in the interpretation of soft cutting: friction, blade geometry, and material response. Separating them is somewhat artificial in that friction can be enhanced in soft materials due to their ability to accommodate large deformation (increased contact area/adhesion). Similarly, blade geometry determines the stress concentration leading to failure, but the stress field varies with the non-linearity of the material response; blade geometry also affects contact area, potentially leading to variations in frictional effects. Nevertheless, these categories

provide a system within which to organize relevant literature with respect to the results we present here.

Contact friction, present in cutting and not tearing, presents a largely unknown component of the measured cutting energy in nearly all of the geometries previously described in the literature. Frictional forces increase as cutting proceeds. Several previous studies addressed this unknown by double-loading a sample, post-cutting, and subtracting the measured load from the purely frictional response from the cutting data at the same displacement [5, 13, 18]. This technique assumes similarities between the two loadings in both contact area and contact force that do not necessarily align. Another approach introduces lubricant at the contacting surface [9, 12]. Lubrication can vary as cutting proceeds and does not reduce the still-large contact area so that some measurable frictional force often remains. By introducing a small tearing component to the applied load, Lake and Yeoh [14] reduced frictional contributions to below the load resolution through reduction of the contact area, essentially only a small region near the blade tip (Fig. 1(c)). Using this approach, one may avoid complications due to friction entirely.

Even the simplest parameterization of a cutting implement requires at least two components, a wedge angle and a tip radius (Fig. 1(b)), though some blades transition between multiple wedge angles [18] and biological cutting tools exhibit almost infinite variety [19], including loss of symmetry. Needle insertion, essentially cutting in a radial rather than planar geometry, contributes even more possibilities for diversity in cutting implements in the form of teeth [20] and medical needles of varying application [21, 22]. While implement geometry affects the measured cutting response, the “sharpness” of an individual blade is not determined by geometry alone for soft, hyperelastic solids [23, Chapter 9]. In other words, the same blade would exhibit a different “sharpness” (determined by cutting force [13, 24, 25] or depth at cutting initiation [18]) depending on the material it was cutting. Further complications arise if

shear forces are introduced (slice/push ratio) [26]; we restrict this work to continuous cutting under normal loads.

Given the complexity observed with the wide variety of available cutting implement geometries [23], space limitations require a brief summary, which we restrict to a few results relevant to the current work. As expected, smaller wedge angles and tip radii result in "sharper" blades with some indication that sharpness is more sensitive to tip radius (according to results from cut initiation in hyperelastic solids [27], needle puncture [22]). For this reason, we vary the blade radius in our experiments.

In elastic-plastic cutting (e.g., metals, wax), radius dependence plateaus at small values of the radius [23, Chapter 9], [28]. One prominent explanation describes blunt blades "pushing a standing wave of metal ahead of the tool" ("ploughing") rather than forming chips [23, Chapter 9]. Some of this material elastically recovers to apply a frictional force to the tool underside as well, further increasing the required load. A sharper blade creates a smaller volume of deformed material ahead of it. A smaller volume of material, relative to the chip size, results in negligible force relative to that required for chip formation and thus the radius dependence plateaus at a value on the order of the chip thickness [23, Chapter 9]. The physical picture of cutting for elastic-plastic materials typically includes a non-contact region ahead of the tool, e.g., the blade has a smaller radius than that of the plastically deformed ''fracture" region leading to chip formation [9, 29, 30]. In contrast, soft, hyperelastic solids like those we discuss here, fully contact the blade tip, no matter the relative geometry of the cutting setup. Blade geometry determines the crack opening profile. However, a material's constitutive response governs the stress-strain distribution around that profile. This article demonstrates cutting's potential capability to characterize fundamental geometry-material interactions by leveraging this crack geometry control.

Crack geometry control is interesting to hyperelastic material failure because these materials exhibit marked crack blunting under far-field loading (e.g., tearing). A crack will blunt when the material modulus is on the same order of magnitude

as the cohesive stress [31]; however, the shape of the blunted crack (and thus the maximum stress) varies with constitutive response [32]. Even assuming linear elastic fracture mechanics, the fracture energy, G_c, of a blunted crack with tip radius, r, at propagation will scale as $G_c \sim rE$, where E is Young's modulus [33]. Key to note is that r is a material parameter, set by the material's modulus and ability to withstand the stress-intensity at the tip. If crack radius alone determined failure, then cutting would always be easier than tearing, opposite of what Lake and Yeoh [14] observed. The relationship between crack geometry and fracture energy for non-linear materials is more complicated. However, controlling crack tip geometry, as is the case during cutting, may provide a mechanism for de-coupling a material's cohesive stress from its constitutive response, thus enabling molecular-structure-based prediction.

Briefly, while we acknowledge that all polymer networks exhibit a time-dependent response, the approach we take here utilizes a highly elastic model system to minimize viscoelastic contributions to the measured failure energy. Previous work on rubbers [14, 15] found that though tearing energy is sensitive to rate, cutting energy is much less so, particularly at lower speeds. We perform tests at low to intermediate speeds to validate these findings in our system. Supported by this combination of efforts, we assume hyperelasticity in our interpretations to follow.

We demonstrate the Y-shaped cutting technique as a method for probing soft material failure. To do so, we first present the simplified expression for cutting energy derived by Lake and Yeoh [14]. We then validate the Y-shaped technique's ability to minimize frictional contributions and to separate tearing and cutting energy contributions for soft silicone elastomers. The latter we find relates to a rate-dependent onset of a stick-slip cutting regime, previously unreported. Finally, we demonstrate the sensitivity of blade-radius-dependent cutting response to a material's constitutive behavior by testing a model system of three silicone elastomers: stiffer/strain-stiffening, softer/neo-Hookean, and softer/strain-stiffening, where the moduli of the softer systems match and the relative stiffening in the strain-stiffening materials match. All

three systems exhibit a plateau in the cutting energy at small radii, but the cutting energy of the neo-Hookean material is much more sensitive to radius than the strain-stiffening systems. We discuss these results in the context of soft failure more generally by comparing the cutting results to tearing tests.

2 Material and Method

2.1 Materials

We investigate three material formulations: two elastomeric networks with differing crosslink density and an elastomeric network diluted by linear polymer chains. The crosslink densities of the elastomers (Sylgard 184, a nanoparticle-toughened PDMS composite, Dow Corning Corp.) are varied by controlling the weight ratio of the pre-polymer base to the curing agent (10:1 and 20:1 (w:w)). Diluted Sylgard 184 materials include 30 wt% trimethylsiloxy terminated linear PDMS (LPDMS) chains (12000-15000 g/mol, 350 cSt, Gelest Inc.) in addition to the 10:1 Sylgard 184. In all cases, the uncured liquid mixtures are mixed in a centrifugal mixer (Speedmixer$^{\text{TM}}$, FlackTek Inc.) at 2000 rpm for 30 seconds before being cast into an acrylic mold. After an additional 10 minute degassing, samples are cured in a thermostat oven at 70°C for 1.75 hours.

2.2 Cutting

The three elastomeric systems are characterized with a Y-shaped cutting method similar to the one outlined in Lake and Yeoh [14]. The customized cutting instrument (Fig. 1(a)) controls sample motion using a motorized test stand (ESM 303, Mark-10®). The cutting blade is mounted on a stationary load cell (M7-05, Mark-10$^{\text{TM}}$, range: $\pm$ 2.5 N, resolution: 5×10^{-4} N) with the cutting edge positioned orthogonally to the sample width. A rectangular sample strip (100 mm $\times$ 15 mm $\times$ 3.2 mm),

including a 40-mm-long precut along its centerline creating two thin legs (legs A) (Fig. 1(b)), is held by the test stand. Hanging weights apply a preload to each of the legs A (Fig. 1(a)). The average pre-stretch ratio in both legs A and B due to the weights is 1.06 ± 0.02 unless otherwise stated. (Sample self-weight is negligible in comparison.) The angle between the legs A is controlled by the symmetric positions of two frictionless pulleys. Most cutting tests are carried out at a rate of 10 mm/min $\pm$ 0.1 mm/min with a leg angle, $2\theta = 80^\circ \pm 1^\circ$. During a cutting test, the test stand displaces the sample toward the razorblade, keeping the leg angle unchanged.

Commercially available blades having as-received or manually blunted geometries are cleaned prior to use. Commercial blades include: feather razorblade (FRB, Feather® Safety Razor), shaving razorblade (SRB, Gillette®, double edge), utility razorblade (URB, GEM®, single edge, uncoated), and trapezoid utility razorblade (TRB, Stanley®). Manual blunting creates blades with a large tip radius (URB blades and a whetstone). Radii (Table 1) are measured by determining the largest possible inscribed circle (ImageJ) within the blade profile imaged via scanning electron microscopy (SEM) (Fig. 1(d) and Fig. S1).

2.3 Standard Mechanical Characterization

The tearing fracture energy of elastomers is measured using a pure-shear, notched tearing test. The apparatus and the procedures for extracting tearing energy are presented in the Supplementary Information (SI) (Fig. S2).

Quasi-static uniaxial tension tests are performed using 'dogbone'-shaped samples following standard test methods for elastomer tension (ASTM D412-16, die D, strain rate: ≈ 0.02 1/s). All samples are stretched until rupture, while measuring load (M7-10, Mark-10™, range: $\pm$ 50 N, resolution: 0.01 N) and strain (video extensometer using fiducial markers).

A DMA instrument (DMA Q800, TA® Instruments) extracts viscoelastic responses using rectangular sample strips (20 mm × 5 mm × 1 mm). Amplitude sweep DMA results find that an oscillation strain amplitude of 1% is well within the linear regime for these materials. Frequency sweeps at this strain amplitude were used to measure the loss tangent ($\tan\delta$). A 5% pre-strain is applied to all frequency sweep samples prior to testing.

3 Determination of Cutting Energy

The Y-shaped cutting geometry consists of a rectangular strip of material into which two "legs" are cut (Fig. 1(b)). A constant force, f_A, loads each of the two legs A, while a force, f_B, is applied to the uncut leg B. A constant angle of separation, 2θ, between the two legs is maintained throughout application of the cutting force, f_{cut}. Lake and Yeoh [14] derived a simple expression to extract the strain energy release rate following energy arguments [33]

$$G = \frac{\partial(U_w - U_{el})}{\partial A} = \lim_{\delta A \to 0} \frac{\delta U_w - \delta U_{el}}{\delta A}, \tag{1}$$

where U_w is the external work done on the sample, U_{el} represents the stored elastic energy, and δA is the change in the fracture surface area. Following a treatment similar to Rivlin and Thomas [34], energy transfer during an infinitesimal increase in crack length is due to work done on and by forces on legs A and B and growth or reduction of the strained material volume in leg B or legs A, respectively. This treatment, which assumes linear elastic behavior of the legs, gives rise to the expression:

$$G_{c,\text{cut}} = \underbrace{\frac{2f_A\bar{\lambda}}{t}(1-\cos\theta)}_{\text{Tearing, } T} + \underbrace{\frac{f_{\text{cut}}\bar{\lambda}}{t}}_{\text{Cutting, } C}, \tag{2}$$

where $\bar{\lambda} = (\lambda_A + \lambda_B)/2$ and t is the sample thickness.[1] Lake and Yeoh denote the first and second terms as "Tearing" and "Cutting", respectively [14]. The tearing term, T, is dominated by the applied load on legs A, f_A and the tearing angle, θ. The cutting force dictates the contribution from the cutting term, C. Although $\bar{\lambda}$ is found in both terms and varies with f_A, θ, and f_{cut}, it does not significantly interrelate T and C. The reason for this is that linear elasticity requires $\bar{\lambda} \approx 1$. Thus, the Y-shaped geometry effectively separates the tearing energy contribution from the cutting energy contribution with the applied θ and the measured f_{cut} determining each term, respectively.

4 Results and Discussion

In this section, we present the advantages of the Y-shaped geometry in reducing frictional effects and demonstrate independent control of cutting versus tearing contributions to failure. We find that this latter control relates to a rate-dependent onset of stick-slip behavior at low cutting speeds (Fig. 5(b)), an effect typically unaddressed in most studies of cutting. We also report for the first time, to our knowledge, on a plateau in cutting energy at small blade radius for rubbery solids that is consistent across multiple, hyperelastic material responses.

4.1 Typical Cutting Response

Typical force-displacement responses of a Y-shaped cutting test (Figure 2) contain three regimes: Initial indentation, cutting, and relaxation. During indentation, the blade reaction force increases until the onset of crack propagation. Upon onset, the force drops, remaining constant throughout continuous cutting. Following Lake and Yeoh [14], we take the maximum value of the force measured within the cutting regime in order to capture the material response that is governed by the most energy

[1] Lake and Yeoh make an unusual and inconsistent approximation in deriving this simple form. We derive the full expression in the Supplementary Information and demonstrate that for the purposes of this manuscript Lake and Yeoh's approximate expression is sufficient.

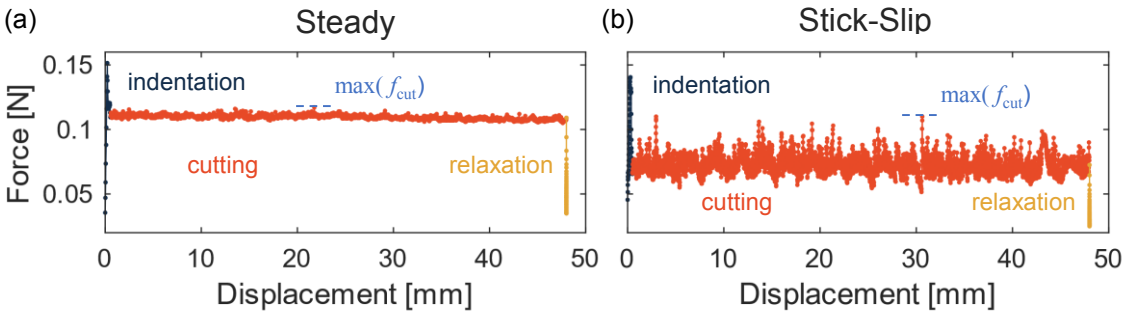

Fig. 2 Typical cutting force-displacement responses. Indentation, cutting, and relaxation regions of the cutting response are denoted by color. (a) A steady cutting response at an intermediate cutting rate (10 mm/min) illustrates a relatively smooth cutting region. (b) At low cutting rate (4 mm/min) a "sawtooth," stick-slip response is observed within the cutting region. Data is for 10:1 Sylgard 184 under the following conditions: URB, $\theta = 40°$.

required to induce failure. Fig. 2 presents two typical curves, one exhibiting a smooth cutting response (Fig. 2(a)) and one at a slower cutting rate showing a jagged response corresponding to stick-slip behavior (Fig. 2(b)). Section 4.4 discusses the rate-dependent transition between these responses in detail. The maximum force within a stick-slip regime and a smooth regime vary little for the materials we tested, even though an average force taken across the entire the cutting regime changes markedly (as evident from Fig. 2). This finding provides further support for the choice of maximum force in determining cutting energy. $G_{c,\text{cut}}$ varied by less than 7% for 10:1 Sylgard 184 tested at a range of cutting rates, 3 mm/min to 100 mm/min, that spanned the transition between regimes (Fig. S3). We combine the measured cutting force with measurements of the leg stretch ratios, λ_A and λ_B, and the applied dead loading, f_A, to calculate $G_{c,\text{cut}}$ using Eqn. (2).

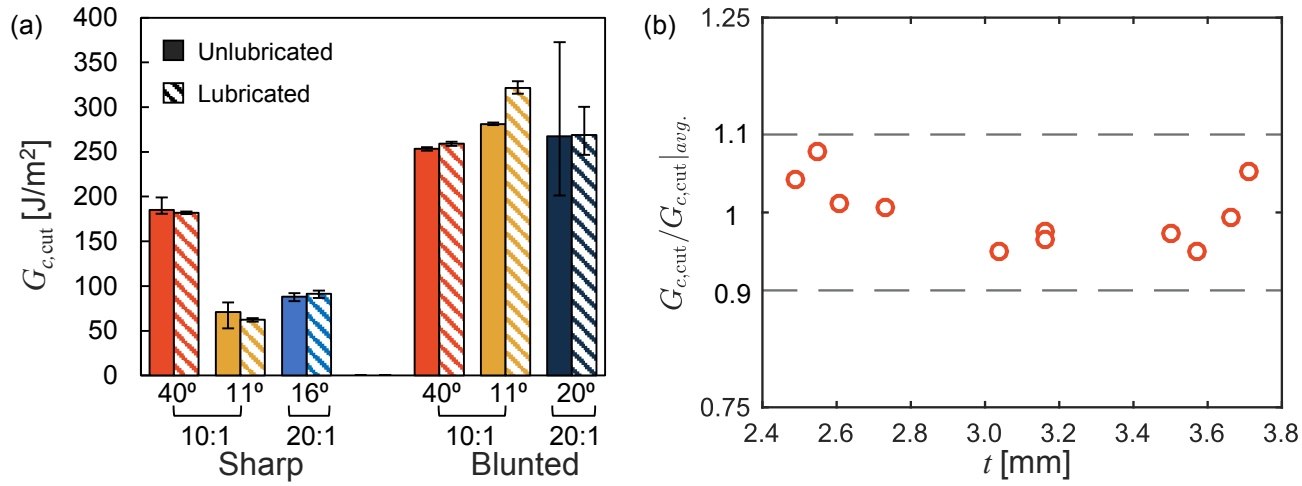

Fig. 3 Evidence for a frictionless assumption. (a) Cutting tests performed with lubricated (stripe) and unlubricated (solid) blades are compared for sharp and blunted blades at varying leg angles, θ. Error bars represent maximum and minimum values from three or more replicates. (Cutting rate: 10 mm/min; Sharp blades: URB; Blunted blades: $r \sim 2000$ nm) (b) Mean-normalized $G_{c,\mathrm{cut}}$ is independent of sample thickness, t. (Razor blade: URB; Cutting rate: 10 mm/min; $\theta = 40°$)

4.2 Minimizing Friction

Overcoming frictional effects requires additional external work, increasing the measured cutting energy typically by an unknown quantity. In using both Y-shaped geometries and stretched crack geometries, Lake and Yeoh [14] demonstrated that frictional effects become negligible for their rubber materials. They attributed this effect to the reduction of the contact area between the material and the razorblade. Here we extend these findings to silicone elastomers an order of magnitude softer than natural rubber. Such materials would be expected to increase contact area due to both adhesive interaction and conformability. Nevertheless, we find that under most conditions (consistent with Lake and Yeoh [14]) frictional effects play a negligible role in the cutting energy (Fig. 3(a)).

We perform two types of experiments to validate “frictionless” measurement. First, cutting tests are performed with lubricated and unlubricated blades. Two radii

(sharp and blunted) and two material formulations (stiffer 10:1 and softer 20:1) are selected for each comparison. Fig. 3(a) summarizes these results. Second, unlubricated tests are performed on samples of varying thickness. In the case of a measurable frictional contribution in the latter, we would expect a monotonically increasing cutting energy as a function of thickness due to the associated increase in contact area. As Fig. 3(b) shows, no such dependence exists. This thickness variation data provides further support for the results of the more efficient lubrication test. Lubrication tests are subject to the critique that lubricant may be used up over a typical 50 mm cutting distance; however, we observe no systematic increase in cutting force as tests progress.

Under most of the conditions tested, we observe no frictional contributions to the cutting energy (Fig. 3). Even in the case of the softest, stickiest material tested, 20:1 Sylgard 184, no statistically significant difference was observed between lubricated and unlubricated tests for a sharp razorblade (URB, see Table 1) with a leg angle as small as 11° or 16°, for stiffer (10:1) and softer (20:1) formulations respectively. These angles are near the blade's half wedge angle of $15^\circ \pm 2^\circ$. (Cutting in not possible in the 20:1 samples for $\theta < 16^\circ$ due to sample buckling. The large force required for cut initiation exceeds the upper limit of $f_{\text{cut}}/f_A = 2\cos\theta$.) Exceptions to these negligible-friction conditions occur when using blunt blades at the lowest leg angle for both sample types (Fig. 3(a), two datasets furthest to the right). At $\theta = 11^\circ$, unlubricated 10:1 samples exhibit a lower $G_{c,\text{cut}}$ than lubricated samples. The increased cutting energy for lubricated blades in the 10:1 material may be due to the increase in blade radius in the presence of a lubrication layer. As we show in subsection 4.5, cutting energy is insensitive to blade radius for sufficiently sharp blades but highly sensitive to radius for blunted blades. The pronounced effect at 11° as opposed to 40° may be related to a transition to a cutting-energy-dominated regime. If so, the radius-dependent cutting force would be anticipated to have a larger contribution to $G_{c,\text{cut}}$. This behavior is consistent with the trends we report later in Section 4.5. In the 20:1

samples, a blunted blade combined with $\theta = 20^\circ$ produces large scatter under both unlubricated and lubricated conditions. Large, infrequent spikes in the load within the cutting regime, different than those characteristic of stick-slip (Fig. 2(b)), suggest that occasional adhesive contact may be responsible for this scatter. The larger error bars associated with the unlubricated tests support this interpretation.

4.3 Controlling Cutting and Tearing Contributions: the Effect of Leg Angle

As with tearing tests, cutting energy can vary with the test geometry and boundary conditions used. We observe that a decrease in angle of separation, θ, corresponds to a decrease in $G_{c,\text{cut}}$ (Figure 4(a)). To understand the origin of this response, we consider the effects of cutting and tearing separately according to Eqn. (2). These contributions are nearly independent when varying θ, as previously noted. Lake and Yeoh [14] observed a transition from a linear proportionality between the two contributions at low tearing energies, T,

$$G_{c,\text{cut}} = \text{const.} = T + C, \tag{3}$$

to an often non-linear, material-dependent relation with increasing T. This regime change tended to correspond to a transition from a smooth (Fig. 2(a)) to stick-slip (Fig. 2(b)) cutting response. They dubbed the linear region a potential "true" cutting regime. In our material system, parameters leading to the onset of stick-slip are more complicated, as will be discussed in detail in the next subsection. This section focuses on the results and implications of experiments on 10:1 Sylgard 184 performed at varying leg splitting angle.

According to Eqn. (2), reducing θ lowers T, but variation in C due to this change is determined solely by the force required to cut the material. Fig. 4(b), shows that for 10:1 Sylgard 184, decreasing T is accompanied by an increase in C that initially fails to compensate for the loss in energy from T (thus the decrease in $G_{c,\text{cut}}$ in Fig. 4(a)); at tearing energies between $\sim$ 75 and 200 J/m^2, the C vs. T slope is

Table 1 Razorblade types, abbreviations, average radii, and half wedge angles.

10:1 Sylgard 184

Razorblade Type	Feather	Shaving	Utility	Trapezoid	Blunted #1	Blunted #2	Blunted #3
Abbreviation	FRB	SRB	URB	TRB	BRB1	BRB2	BRB3
Radius [nm]	37	86	127	253	528	2080	5092
Half-angle [°]	16 ± 1	14.4 ± 0	14.7 ± 0.8	15.0 ± 0.3	14.7 ± 0.8	14.7 ± 0.8	14.7 ± 0.8

10:1-diluted and 20:1 Sylgard 184

Razorblade Type	Feather	Shaving	Utility	Trapezoid	Blunted #4	Blunted #5
Abbreviation	FRB	SRB	URB	TRB	BRB4	BRB5
Radius [nm]	39	83	131	245	198	519
Half-angle [°]	16 ± 1	14.4 ± 0	14.7 ± 0.8	15.0 ± 0.3	14.7 ± 0.8	14.7 ± 0.8

less than 1 (≈ -0.23). A transition to a higher magnitude slope at lower tearing energies (Fig. 4(b)) appears to approach Lake and Yeoh's "true" cutting energy relation (Eqn. (3)). Fig. 4(b) illustrates this finding with a best-fit line having a slope of -1 (dashed). Interestingly, the magnitude of the tearing energy at which the transition occurs is less than half the value reported by Lake and Yeoh (~ 200 J/m^2) which they found to be consistent for all natural and styrene-butadiene rubbers (with and without filler) tested. With all of our data falling below this energy threshold, combined with our observations of smooth cutting responses (Fig. 2(a)) for all data used to generate Fig. 4(b), it would be tempting to categorize any point in Fig. 4(b) as "true" cutting. The idea motivating use of the characteristic cutting response to indicate onset of a "true" cutting is that stick-slip indicates the presence of "induced" tearing events (i.e., the temporary loss of material resistance to crack propagation). Fig. 4(b) illustrates the importance of a series of tests for finding the transition to the linear relation in Eqn. (3). It may be that viscoelastic effects, though minimal, sufficiently suppress

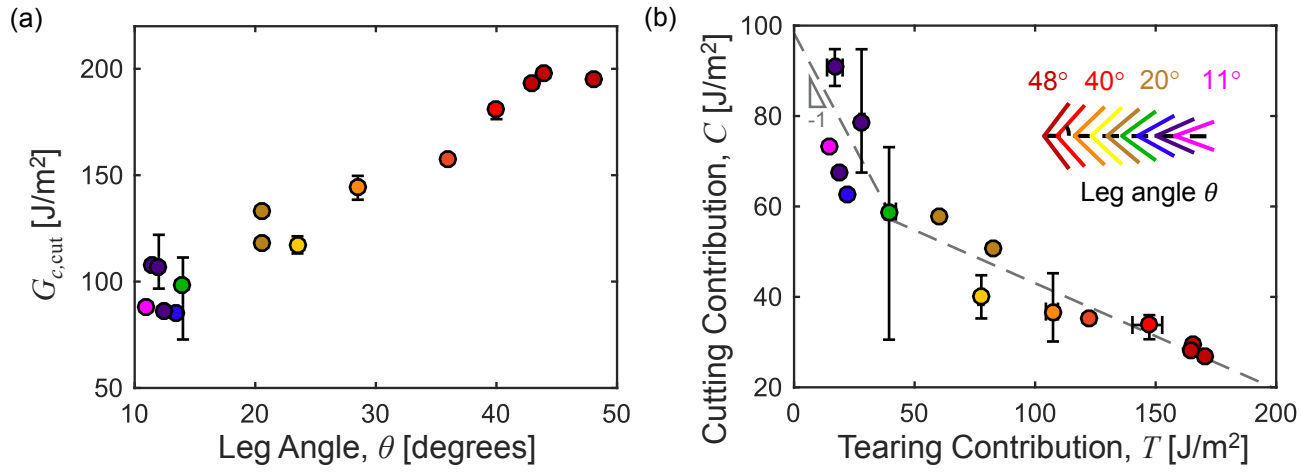

Fig. 4 Test geometry variation for control of C and T. Cutting is performed at 10 mm/min. (a) $G_{c,\mathrm{cut}}$ increases monotonically with leg angle, θ. (b) The variation in C as a function of T transitions between two regimes. The fit (dashed line) on the left has a fixed slope of -1, indicative of "true" cutting. A linear fit at higher T yields a slope of -0.23. Error bars represent maximum and minimum values of three or more samples. (Razorblade: SRB, except the three datapoints furthest to the right in both plots, which use URB. Both SRB and URB blades lie within the plateau region of Fig. 6, and thus can be plot together despite their small variation in r.)

rapid tearing in our system. At low cutting rates where "induced" tearing is observed, suppression of the stick-slip response can be achieved by a reduction in θ. We discuss this and other rate-dependent effects in the next section.

More experiments may be necessary to determine the conditions required to transition to the "true" cutting regime. Without reported modulus values for comparison with Lake and Yeoh, we must speculate that 10:1 Sylgard 184's lower transition point derives from either reduced toughness, reduced modulus or both. The ratio of the two contributions (C/T) at onset is inconsistent as well; in our data $C/T \approx 1.5$ for Lake and Yeoh, $C/T \approx 0.3$. We conclude that the transition between cutting and tearing dominated regimes must currently be experimentally determined for each material type if a "true" cutting response (Eqn. (3)) is desired.

Note that our aim with this cutting setup is the extraction of setup-geometry-independent material properties. Both the onset of the linear regime and the intercept at $T = 0$ are potential candidates, but require further characterization outside of the scope of this manuscript. Presently, interference from contact effects at small θ prevent replication of Fig. 4(b) for softer formulations. Blade radius likely alters behavior as well (see subsection 4.5). In spite of these limitations, Fig. 4(b) illustrates that the $G_{c,\text{cut}}$ dependence observed in Fig. 4(a) can be quantitatively understood as an overall dominance of the tearing contribution in this sample geometry which we would expect to see in cutting tests more generally. There appears to be an excess of tearing energy available, but not strictly necessary, for local material failure. On a related note, very brittle materials (e.g., polyacrylamide hydrogels) are challenging to cut as even a small tearing contribution induces catastrophic tearing that eliminates the opportunity for steady-state cutting.

4.4 Rate Dependence of the Cutting Response

Rate dependence observed in the cutting responses of each of the three model materials originates from bulk viscoelasticity and what may be a viscoelasticity-governed, failure-related timescale associated with crack tip progression. To clarify what we mean by each of these two mechanisms, we consider bulk viscoelasticity to determine the polymer chain reorientation-governed time dependence of the stress-strain distribution outside of the fracture process zone. The failure-related timescale is hypothesized to relate to possible local chain pull-out, void formation and coalescence, or other microstructure-based, pre-failure processes within the fracture process zone. We believe the first effect to be minimal for our materials and report on the observations that lead to the second conclusion.

Understanding the role of viscoelastic effects in cutting is not the focus of this work. For this reason, we chose materials that were highly elastic. Fig. 5(a) summa-

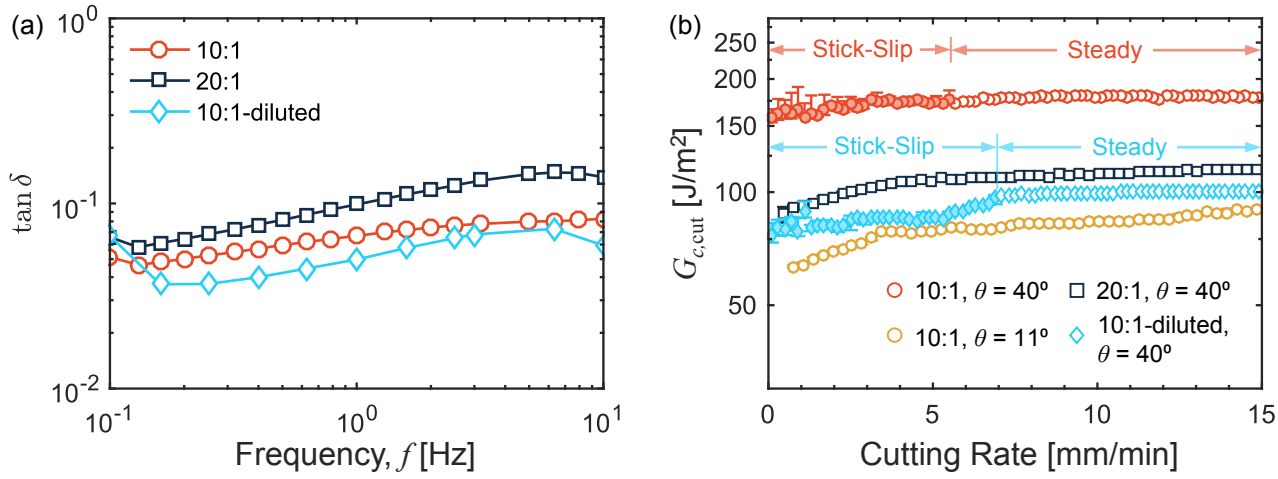

Fig. 5 Rate dependence. (a) DMA frequency sweeps demonstrate highly elastic behavior for all three materials: 10:1 (orange circles), 20:1 (blue squares), and 10:1-diluted (cyan diamonds). (b) Speed sweep tests illustrate the onset of stick-slip behavior via a plot of $G_{c,\mathrm{cut}}$ versus cutting rate. The stick-slip regimes are highlighted with filled symbols, while unfilled symbols represent the steady regime. Cutting Rate changes at a rate of 2.16 mm/min^2. $G_{c,\mathrm{cut}}$ is evaluated within an interval of 0.2 mm/min. Error bars indicate the spread in local maxima within the interval.

rizes the linear viscoelastic responses for all three materials: 10:1 (orange circles), 20:1 (navy squares), and 10:1-diluted (cyan diamonds), obtained using DMA. Over the range of frequencies tested, the viscous component is relatively small as noted by the dissipation factor, $\tan\delta = E_{\mathrm{loss}}/E_{\mathrm{storage}} < 0.1$. E_{storage} and E_{loss} are the storage and loss moduli, respectively. To understand to what degree these viscous dissipation values may affect the highest strain rates during cutting requires two estimates: one for the approximate strain rate at a given frequency and one for the strain gradient near the blade tip.

Approximating the DMA strain rate requires homogenization of the sine-wave loading rate; estimating the strain gradient is more difficult. The average DMA strain

rate is calculated as

$$\left.\frac{d\varepsilon_{\mathrm{DMA}}}{dt}\right|_{\mathrm{avg.}} = \frac{\int_0^{\frac{1}{2f}} \frac{d\Delta h}{dt} dt}{h/2f} = 4\varepsilon_{\mathrm{amp}} f, \tag{4}$$

where Δh is the nominal displacement from the initial length sample length, h, f is the oscillation frequency, and $\varepsilon_{\mathrm{amp}}$ is the oscillation strain amplitude. It follows that 0.1 Hz corresponds to 4×10^{-3} 1/s and 10 Hz corresponds to 0.4 1/s for the conditions in Fig. 5(a) ($\varepsilon_{\mathrm{amp}} = 0.01$). As a first approximation for determining the strain rate under the blade tip, we draw upon indentation strain rate measurements [35]; the tip displacement rate is divided by the displacement depth. For a typical cutting speed (10 mm/min) and an estimated indentation depth of 1 mm, this yields 0.167 1/s (4.175 Hz in Fig. 5(a)). We obtain another approximation using digital image correlation (DIC) (see SI) to obtain the strain distribution in the region approaching the blade tip (Fig. S5(b)). Under steady-state cutting conditions, a derivative of the strain with respect to distance from the blade tip, d, is multiplied by cutting speed to obtain the instantaneous strain rate at each point ahead of the tip (Eqn. (S2), Fig. S5(c)). The maximum strain rate determined in this way is ~ 0.02 1/s at $d \approx 0.6$ mm (0.5 Hz in Fig. 5(a); DIC resolution decays at $d < 0.6$ mm). Both estimated strain rates, in the regions under and approaching the blade tip, correspond to frequencies suggesting that the viscous contribution remains low for the reported data.

Cutting tests using the Y-shaped geometry appear to minimize viscoelastic contributions in general. As previously mentioned, over rates ranging from 3 – 100 mm/min, only a 7% variation in $G_{c,\mathrm{cut}}$ is observed for 10:1 Sylgard 184 (Fig. S3) despite the fact that at 100 mm/min we might expect sizable viscous effects (strain rate of ~ 1.67 1/s (41.67 Hz)). Similarly, Gent, et al. [15] found that for their rubber formulation at room temperature, cutting energy was nearly constant over two orders of magnitude change in cutting speed. In comparison, tearing energy under similar conditions increased by nearly an order of magnitude. In other words, the larger crack tip deforma-

tions seen in tearing tests, which would be governed by bulk viscoelasticity effects, are minimal in the Y-shaped cutting geometry. This benefit likely does not hold for all cutting geometries, especially in soft materials that might adhere to the cutting implement during testing (e.g., needle puncture). In such cases, stress concentrations may be effectively lessened by adhesion (which would restrict relative deformation at the cutting interface) and consequently require larger deformation. Large deformation means larger deformed volumes and thus a greater influence of viscoelastic effects. This physical description is not the case for the contact-area reducing geometry we apply here.

Although rate plays a minor role in the cutting energy, it noticeably affects the observed cutting response. Continuous cutting responses fall into two categories: smooth and stick-slip (Fig. 2(a) and 2(b), respectively). The transition between these two types of cutting occurs as a function of the cutting rate used; we observe the "saw-tooth pattern" at lower rates. To determine the onset of the stick-slip cutting regime, we perform speed sweep tests (Fig. 5(b)). In a speed sweep test, the cutting speed ranges continuously between 0 and 15 mm/min and the onset of the stick-slip regime occurs when scatter in the cutting force value is visible (filled symbols). $G_{c,\mathrm{cut}}$ and the scatter derive from the mean and the spread in the local force maxima within a 0.2 mm/min speed interval. Stick-slip always corresponds to a lower mean cutting force, though the maximum force remains relatively unchanged (Fig. S3). Thus, Fig. 5(b) illustrates an apparent, but not real, decrease in $G_{c,\mathrm{cut}}$ within the stick-slip regime.

The onset of this stick-slip cutting behavior is not fully understood. While it appears linked to a failure-related timescale, the relative contribution of the cutting and tearing components affect its onset as well. As evidenced in Fig. 5(b), onset of stick-slip occurs at $\sim$ 7 mm/min and $\sim$ 5.5 mm/min for 10:1-diluted (cyan diamonds) and 10:1 (orange circles) samples, respectively (test conditions: $\theta = 40^\circ$ and $\bar{\lambda} = 1.06 \pm 0.02$). We observe no stick-slip response for the 20:1 formulation over the range of cutting speeds tested. Qualitative comparison with Fig. 5(a) shows that the

decreasing stick-slip onset rate corresponds to increasing viscoelasticity. We speculate that local failure processes, which would be expected to influence the timescale of damage evolution at the crack tip, may be governed by polymer chain motion similar to that giving rise to viscoelasticity. Another possibility may be local adhesive contact between the material and blade that prevents rapid crack propagation, 20:1 being sticker than both 10:1 formulations. In what might at first appear at odds with these observations of a rate-dependent onset, Lake and Yeoh [14] described the transition to stick-slip as occurring under higher T (lower C) test conditions that "induced" tearing. At low T, in the "true" cutting regime, the stick-slip is suppressed. We also observe that changes in the angle between the legs, θ, alter stick-slip onset in a way that qualitatively mimics Lake and Yeoh's results. As Fig. 5(b) shows, a reduction of θ, corresponding to decreasing T, produces a speed sweep curve with no visible stick-slip response. Thus, we also suppress stick-slip over the range of rates tested given sufficiently low tearing contributions. We conclude that the onset of stick-slip depends on both material properties and loading conditions and requires further study to determine the relative weight of these factors.

4.5 Blade Radius-Dependent Cutting Energy

Despite its applicability to a broad range of test conditions, Eqn. (2) does not account for the effect of blade geometry on the measured cutting energy. Lake and Yeoh [14] acknowledged an approximate proportionality between blade thickness near the tip and cutting energy for the range of blades available at that time. This linear proportionality is reminiscent of fracture scaling arguments $G_c \sim rE$, and notch sensitivity arguments, $G_c \sim rW_B$ [36]. (Here r refers to the crack or notch radius and W_B is the work to break an un-notched sample). However, to our knowledge, a systematic study of the effect of blade radius, r, on the energy required to continuously cut soft materials has never been reported. Most cutting tool geometry studies focus on cut *initiation*

[18, 25] or puncture [37–39] and few systematically vary over several radii. Here we report a universal behavior at small radius observed in all three materials and for two leg angles in the stiffer material. We also find that the relation between $G_{c,\text{cut}}$ and r at larger radius relates to the material's strain-stiffening response.

The following cutting experiments avoid frictional and rate-dependent effects by accommodating the technique's current limitations, as explored in the previous sections. Unless otherwise stated, results in this subsection were gathered at 10 mm/min with $\theta = 40^\circ$ and $\bar{\lambda} \approx 1.06 \pm 0.02$. Tests employ blade radii that vary by two orders of magnitude (Table 1) measured using scanning electron microscopy. Wedge angle is approximately constant ($\sim 15^\circ$) across all blades. Fig. 6(a) shows the results for all three materials: 10:1, 10:1-diluted, and 20:1. For the stiffest material, 10:1, a second set of data (light orange circles) reports the effect of tearing angle for tests performed at $\theta = 31^\circ$. As previously mentioned and illustrated by Fig. 6(b), the set of model materials provides comparisons between

- Materials with similar strain-stiffening, but different elastic modulus. (10:1 has a greater modulus than 10:1-diluted.)
- Materials with similar small-strain modulus, but with or without strain-stiffening (10:1-diluted and 20:1, respectively).

In all cases, there exists a "threshold" cutting regime when the blade tip decreases below a critical length scale. In this regime, the cutting energy plateaus despite the use of a "sharper" blade (Fig. 6(a)). Typically we expect sharper blades to produce a higher stress-concentration, leading to earlier failure. At present, we can only speculate on what length scale sets this transition. It seems unlikely the length scale is set by the elasto-cohesive length scale, G_c/E, discussed by Creton and Ciccotti [33]. For these materials the elasto-cohesive length is much larger, on the order of 100 μm or more (See SI). One explanation postulated by Tony Atkins [23, Chapter 9] suggests that the reason sharper tools may not decrease the necessary crack prop-

agation energy is that they only intensify stress within a highly localized volume. This volume is too small to encompass the microstructural features that control fracture, therefore a cutting force sufficient to increase the local deformed volume to a threshold level must be reached. In the Sylgard 184-based materials system we use, the most apparent microstructural length scales arise from the elastomer network and the silica nanoparticles. Using the entanglement molecular weight of PDMS as an upper limit, one can estimate a crosslink spacing of 7 nm. For $\sim$50 nm radius silica aggregates occupying a volume fraction of $\gtrsim 0.16$ [40], we calculate a 50 nm (70 nm for 10:1-diluted) interaggregate spacing for all materials (See SI). If the minimal microstructure hypothesis is correct, it seems most likely that silica filler, rather than the network size, plays a critical role in the failure process as the transition to the threshold regime occurs between 200 – 300 nm, on the order of a few aggregates. The similarity in the length scale at which the plateau occurs for all samples would then be due to the material's microstructural similarity. Further tests on unfilled material formulations could verify this hypothesis.

Though all materials and leg angles exhibit a threshold behavior, the threshold value differs. The two similar Young's modulus materials (10:1-diluted, 0.4 MPa and 20:1, 0.3 MPa) produce nearly identical plateau values, while the 10:1 samples, having a 3-fold larger modulus, exhibit only a 2-fold increase in the plateau $G_{c,\mathrm{cut}}$ for the same leg angle. We note that a stiffer material exhibiting higher toughness is opposite the behavior predicted by the Lake-Thomas model [41], which, however, applies primarily to unfilled networks. Swelling tests (see SI) suggest that 20:1 has the lowest crosslink density (swelling ratio (Q) = 4.3), followed by 10:1-diluted (Q = 3.0) and 10:1 (Q = 2.5). Based on this information, Lake-Thomas theory predicts the highest tearing energy accompanies 20:1. Nanoparticle interaction likely plays a role here. In the materials tested, variation in nanoparticle content [40] is relatively small. (The volume fraction of 20:1 is $\sim$5% larger than 10:1 and $\sim$50% larger than 10:1-diluted, see SI). At low crosslink densities, tearing energy in carbon-black filled SBR has

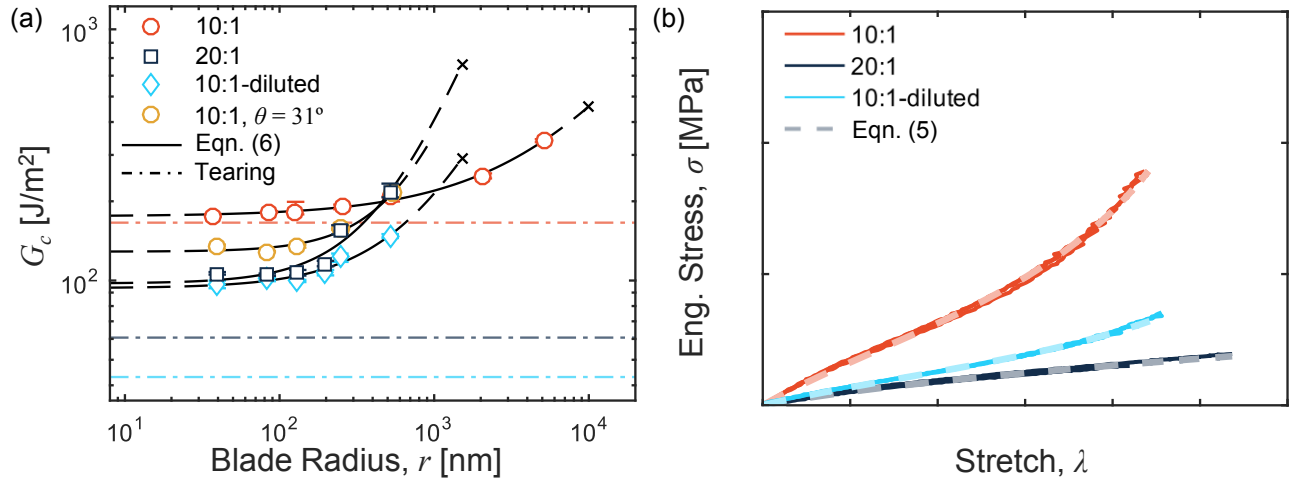

Fig. 6 Radius and material dependence. (a) As blade radius decreases, G_c decreases until it plateaus at a threshold radius value for all four material and leg angle conditions: 10:1 ($\theta = 40°$, orange circles), 10:1 ($\theta = 31°$, light orange circles), 20:1 ($\theta = 40°$, blue squares), and 10-1 diluted ($\theta = 40°$, cyan diamonds). Dashed and solid lines represent the extrapolated fit and fit curves, respectively, using Eqn. (6). The cross marker on each curve indicates the limit at which cutting was attempted but not possible. Light-colored dash-dot lines indicate pure-shear tearing energy, with colors matching the corresponding materials'. Error bars represent maximum and minimum values from four or more replicates. (Cutting rate: 10 mm/min.) (b) Uniaxial tension responses (saturated lines) are fit using the Gent model (lighter dashed lines). Three samples are characterized for each material. Gent fits are generated by averaging the experimental curve fit results.

been found to increase with increasing crosslink density/stiffness for constant filler content [42]. This would explain why 10:1 has the highest plateau $G_{c,\text{cut}}$. Increased nanoparticle content toughens elastomers more generally [43]. Thus, the combined effects of higher nanoparticle content and larger molecular weight between crosslinks may be responsible for 20:1 having a larger plateau $G_{c,\text{cut}}$ than 10:1-diluted. Quasistatic pure shear tests (Fig. 6a, dash-dot lines) agree qualitatively with the plateau cutting energy value at 40° for all three materials. For all 40° curves, we find that the plateau cutting energy is greater than the tearing energy from pure shear. For the reduced leg angle, $\theta = 31°$, this relationship no longer holds. As we might expect

from Fig. 4a, the cutting energy decreases with decreasing leg angle. It may be that smaller angles begin to approach a material threshold value for the cutting energy. Pure shear tests were not verified as threshold tear values [44], but were simply performed at the slowest practical strain rate, 0.002 1/s. A relationship between cutting and tearing threshold energies will require further tear testing and development of the cutting technique. Currently, practical limitations prohibit gathering full radius-dependence curves for smaller leg angles. At larger blade radii, we observe variation with material type, evidence of the material-dependent "sharpness" effect observed by others [13, 18, 23–25].

The material-dependent response at large blade radius provides evidence that, by minimizing contact-related deformation and frictional effects, the Y-shaped geometry is a means for exploring and establishing a relationship between a material's cutting behavior and its far-field loaded tearing response. As Fig. 6(a) shows, the sensitivity of $G_{c,\text{cut}}$ to r is largest for a non-strain stiffening material, 20:1 (Fig. 6(b), dark blue), or a smaller leg angle (Fig. 6(a), light orange circles). To study these effects quantitatively, we parameterize the materials' stress-strain responses and fit $G_{c,\text{cut}}$ versus r. We find that, while an incompressible neo-Hookean response accurately describes the 20:1 material (coefficient of determination, $R^2 = 0.995$), an incompressible Gent model [45],

$$\sigma = \left(\lambda - \frac{1}{\lambda^2}\right)\left(\frac{\mu J_{\text{lim}}}{J_{\text{lim}} - I_1 + 3}\right) \tag{5}$$

was necessary to capture the strain-stiffening of the 10:1 and 10:1-diluted samples. Here shear modulus, μ, and J_{lim} are the fit parameters, σ and λ are the uniaxial engineering stress and stretch, respectively, and $I_1 = \lambda^2 + 2/\lambda$ is the first invariant. Smaller J_{lim} indicates an earlier onset of strain-stiffening. From earliest to latest, the strain-stiffening response of the materials is ordered: 10:1, $J_{\text{lim}} = 3.7 \pm 0.2$; 10:1-diluted, $J_{\text{lim}} = 4.8 \pm 0.4$; and 20:1, $J_{\text{lim}} = (1.7 \pm 0) \times 10^6$. (The ranges reflect standard deviations across three samples.) As anticipated, 20:1 samples exhibit non-strain-

stiffening behavior via an extremely large J_{lim} value. (Gent and neo-Hookean models become equivalent for $J_{\text{lim}} \to \infty$.) For comparison, we fit a power-law relation of the form,

$$G_{c,\text{cut}} = G_{\text{threshold}} + ar^n, \tag{6}$$

to quantify the degree of $G_{c,\text{cut}}$ sensitivity, n, to blade radius. The exponents, n, in order of increasing sensitivity:10:1, $n = 0.808 \pm 0.006$; 10:1-diluted, $n = 1.19 \pm 0.04$; and 20:1, $n = 1.44 \pm 0.04$, directly correspond to a decrease in the onset of strain-stiffening. (The ranges reflect 95% confidence intervals.) The smallest angle 10:1 curve (Fig. 6(a), light orange circles) exhibits the largest sensitivity to radius, $n = 1.60 \pm 0.03$, illustrating that boundary conditions effect n as well. Note that all of these values are near one as observed by Lake and Yeoh and suggested by the scaling relations $G_c \sim rE$ and $G_c \sim rW_B$, but none is equal to one.

Both practical implications and physical understanding follow from the one-to-one correspondence between $G_{c,\text{cut}}$ sensitivity and strain-stiffening. If using cutting as a metrology technique, while ignoring blade radius, a strain-stiffening material with a higher threshold cutting energy might be observed to have the same cutting energy as another material that exhibits little strain-stiffening. Take for example the cross-over between 10:1 and 20:1 curves at $r \approx 500$ nm (Fig. 6(a)). The softer, lower threshold $G_{c,\text{cut}}$, 20:1 material might be characterized as the tougher material if using a larger radius blade. Distinguishing materials even closer in behavior would be especially challenging, even with blades approaching the $\sim$200 nm radius sharpness threshold. Qualitatively we interpret this result as follows. A non-strain-stiffening material more easily accommodates the deformation required by large radius blade. Thus, the energy contribution from cutting must be larger, e.g., requiring a higher cutting force, for an incremental increase in radius since the material itself is not storing the required energy. This interpretation is supported by the 31° data, which exhibits the largest radius sensitivity of all. The lower applied tearing energy reduces

the strain near the blade, which reduces the stiffness in that local region. This deformability in turn more readily accommodates larger radius blades. Again, the energy contribution from cutting must be larger for an incremental increase in radius, as we observe. While we have demonstrated two ways in which the Y-shaped cutting test provides insight relevant to a material's tearing behavior, the picture remains incomplete. Quantitatively linking cutting and tearing energy is a complex task requiring more experience with the Y-shaped test setup and a further variety of material responses.

5 Summary and Conclusions

We present results from and limitations of a promising, but under-utilized Y-shaped cutting geometry originally presented by Lake and Yeoh [14]. For the first time, we extend this technique to soft samples that exhibit crack-blunting under far-field loading conditions. We show that even in these highly deformable and often adhesive systems, the technique retains its ability to eliminate frictional effects and tune the relative cutting and tearing contributions to the energy driving fracture. Two new observations are reported.

We report on an additional mechanism for eliminating the "sawtooth" stick-slip response during cutting and show that cutting energy dependence on blade radius is non-linear. Onset of the "sawtooth" cutting response was previously reported to accompany a transition from low to high tearing energy test conditions [14]. We further demonstrate that the stick-slip response is suppressed at sufficiently high, though still moderate, cutting rate for the materials we tested. The physical processes controlling the nature and onset of stick-slip remain an area for future study. Second, experiments varying blade radius illustrate a transition, near a blade radius of 200 nm, to a threshold value for the cutting energy in all three materials. Previously it was thought that cutting energy would decrease proportionally with blade radius, due to either stress

concentration effects or scaling relations that describe far-field tearing conditions. Rather, it appears that cutting produces a blade-geometry-independent response for a sufficiently sharp blade. This plateau response also remains unchanged as a function of leg tearing angle (at least for one material formulation). Prediction of sufficient sharpness and the material and geometric parameters that govern it will require both mechanical and microstructural considerations. Blunter blades, on the other hand, provide a link between crack tip geometry and the material's strain stiffening response that merits exploration as a controlled system for understanding the effect of material non-linearity on soft fracture in the presence crack-blunting. These avenues for future work will provide the knowledge necessary to link cutting and tearing failure energies in soft materials quantitatively.

Acknowledgements This material is based upon work supported by the National Science Foundation under grant no. 1562766. DMA tests were performed in the Frederick Seitz Materials Research Laboratory Central Research Facilities, University of Illinois. Some SEM images were gathered in the Beckman Institute for Advanced Science and Technology, University of Illinois. The authors thank Bryan Bunch and Andrew Dou for their contributions to the experimental data set.

References

1. Shih AJ, Lewis MA, Strenkowski JS (2004) End Milling of Elastomers-Fixture Design and Tool Effectiveness for Material Removal. Journal of Manufacturing Science and Engineering 126(1):115. https://doi.org/10.1115/1.1616951
2. Chanthasopeephan T, Desai JP, Lau AC (2006) Determining fracture characteristics in scalpel cutting of soft tissue. Proceedings of the First IEEE/RAS-EMBS International Conference on Biomedical Robotics and Biomechatronics, 2006, BioRob 2006 2006:899–904. https://doi.org/10.1109/BIOROB.2006.1639205
3. Chanthasopeephan T, Desai JP, Lau AC (2007) Modeling soft-tissue deformation prior to cutting for surgical simulation: Finite element analysis and study of cut-

ting parameters. IEEE Transactions on Biomedical Engineering 54(3):349–359. https://doi.org/10.1109/TBME.2006.886937

4. Freeman PW, Lemen CA (2007) The trade-off between tooth strength and tooth penetration: Predicting optimal shape of canine teeth. Journal of Zoology 273(3):273–280. https://doi.org/10.1111/j.1469-7998.2007.00325.x
5. Lucas PW, Pereira B (1990) Estimation of the fracture toughness of leaves. Functional Ecology 4(6):819–822. https://doi.org/10.2307/2389448
6. Pereira BP, Lucas PW, Swee-Hin T (1997) Ranking the fracture toughness of thin mammalian soft tissues using the scissors cutting test. Journal of Biomechanics 30(1):91–94. https://doi.org/10.1016/S0021-9290(96)00101-7
7. Darvell BW, Lee PK, Yuen TD, Lucas PW (1996) A portable fracture toughness tester for biological materials. Measurement Science and Technology 7(6):954–962. https://doi.org/10.1088/0957-0233/7/6/016
8. Ericson M, Lindberg H (1996) A method of measuring energy dissipation during crack propagation in polymers with an instrumented ultramicrotome. Journal of Materials Science 31:655–662. https://doi.org/10.1007/BF00367882
9. Patel Y, Blackman BR, Williams JG (2009) Determining fracture toughness from cutting tests on polymers. Engineering Fracture Mechanics 76(18):2711–2730. https://doi.org/10.1016/j.engfracmech.2009.07.019
10. Chang L, Wang H (2013) Cutting Tests: A New Method to Determine the Fracture Toughness of Polymeric Materials. Journal of Applied Mechanical Engineering 2(1):2–3. https://doi.org/10.4172/2168-9873.1000e110
11. Williams JG, Atkins AG, Charalambides MN, Lucas PW (2016) Cutting science in biology and engineering. Interface Focus 6(3):1–2. https://doi.org/10.1098/rsfs.2016.0021
12. Willis A, Vincent JF (1995) Monitoring cutting forces with an instrumented histological microtome. Journal of Microscopy 178(1):56–65. https://doi.org/10.1111/j.1365-2818.1995.tb03581.x

13. Brown T, James SJ, Purnell GL (2005) Cutting forces in foods: Experimental measurements. Journal of Food Engineering 70(2):165–170. https://doi.org/10.1016/j.jfoodeng.2004.09.022
14. Lake GJ, Yeoh OH (1978) Measurement of rubber cutting resistance in the absence of friction. International Journal of Fracture 14(5):509–526. https://doi.org/10.1007/BF01390472
15. Gent AN, Lai SM, Nah C, Wang C (1994) Viscoelastic Effects in Cutting and Tearing Rubber. Rubber Chemistry and Technology 67(4):610–618. https://doi.org/10.5254/1.3538696
16. Gent AN, Wang C (1996) Cutting resistance of polyethylene. Journal of Polymer Science, Part B: Polymer Physics 34(13):2231–2237. https://doi.org/10.1002/(SICI)1099-0488(19960930)34:13<2231::AID-POLB12>3.0.CO;2-6
17. Atkins AG, Mai YW (1979) On the guillotining of materials. Journal of Materials Science 14(11):2747–2754. https://doi.org/10.1007/BF00610649
18. McCarthy CT, Hussey M, Gilchrist MD (2007) On the sharpness of straight edge blades in cutting soft solids: Part I indentation experiments. Engineering Fracture Mechanics 74:2205–2224. https://doi.org/10.1016/j.engfracmech.2009.10.003
19. Anderson PSL, LaBarbera M (2008) Functional consequences of tooth design: effects of blade shape on energetics of cutting. Journal of Experimental Biology 211(22):3619–3626. https://doi.org/10.1242/jeb.020586
20. Schofield RM, Choi S, Coon JJ, Goggans MS, Kreisman TF, Silver DM, Nesson MH (2016) Is fracture a bigger problem for smaller animals? Force and fracture scaling for a simple model of cutting, puncture and crushing. Interface Focus 6(3). https://doi.org/10.1098/rsfs.2016.0002
21. Han P, Che D, Pallav K, Ehmann K (2012) Models of the cutting edge geometry of medical needles with applications to needle design. International Journal of Mechanical Sciences 65(1):157–167. https://doi.org/

10.1016/j.ijmecsci.2012.09.014

22. Nguyen CT, Vu-Khanh T, Dolez PI, Lara J (2009) Puncture of elastomer membranes by medical needles. Part I: Mechanisms. International Journal of Fracture 155(1):75–81. https://doi.org/10.1007/s10704-009-9326-7
23. Atkins T (2009) The Science and Engineering of Cutting: The Mechanics and Processes of Separating, Scratching and Puncturing Biomaterials, Metals and Non-metals. Butterworth-Heinemann. https://doi.org/https://doi.org/10.1016/C2009-0-17178-7
24. Zhou D, McMurray G (2010) Modeling of blade sharpness and compression cut of biomaterials. Robotica 28(2):311–319. https://doi.org/10.1017/S0263574709990385
25. Schuldt S, Arnold G, Kowalewski J, Schneider Y, Rohm H (2016) Analysis of the sharpness of blades for food cutting. Journal of Food Engineering 188:13–20. https://doi.org/10.1016/j.jfoodeng.2016.04.022
26. Atkins AG, Xu X (2005) Slicing of soft flexible solids with industrial applications. International Journal of Mechanical Sciences 47(4-5 SPEC. ISS.):479–492. https://doi.org/10.1016/j.ijmecsci.2005.01.013
27. McCarthy CT, Annaidh AN, Gilchrist MD (2010) On the sharpness of straight edge blades in cutting soft solids: Part II - Analysis of blade geometry. Engineering Fracture Mechanics 77(3):437–451. https://doi.org/10.1016/j.engfracmech.2009.10.003
28. Kountanya RK, Endres WJ (2004) Flank Wear of Edge-Radiused Cutting Tools Under Ideal Straight-Edged Orthogonal Conditions. Journal of Manufacturing Science and Engineering 126(3):496. https://doi.org/10.1115/1.1765148
29. Williams JG (1998) Friction and plasticity effects in wedge splitting and cutting fracture tests. Journal of Materials Science 33(22):5351–5357. https://doi.org/10.1023/a:1004490015211

30. Williams JG, Patel Y (2016) Fundamentals of cutting. Interface Focus 6(3). https://doi.org/10.1098/rsfs.2015.0108
31. Hui CY, Jagota A, Bennison SJ, Londono JD (2003) Crack blunting and the strength of soft elastic solids. Proceedings of the Royal Society A: Mathematical, Physical and Engineering Sciences 459(2034):1489–1516. https://doi.org/10.1098/rspa.2002.1057
32. Long R, Hui CY (2015) Crack tip fields in soft elastic solids subjected to large quasi-static deformation - A review. Extreme Mechanics Letters 4:131–155. https://doi.org/10.1016/j.eml.2015.06.002
33. Creton C, Ciccotti M (2016) Fracture and adhesion of soft materials: a review. Reports on Progress in Physics 79(4):046601. https://doi.org/10.1088/0034-4885/79/4/046601
34. Rivlin RS, Thomas AG (1953) Rupture of rubber. I. Characteristic energy for tearing. Journal of Polymer Science 10(3):291–318. https://doi.org/10.1002/pol.1953.120100303
35. Lucas BN, Oliver WC (1999) Indentation power-law creep of high-purity indium. Metallurgical and Materials Transactions A 30(3):601–610. https://doi.org/10.1007/s11661-999-0051-7
36. Thomas AG (1955) Rupture of rubber. II. The strain concentration at an incision. Journal of Polymer Science 18(88):177–188. https://doi.org/10.1002/pol.1955.120188802
37. Fakhouri S, Hutchens SB, Crosby AJ (2015) Puncture mechanics of soft solids. Soft Matter 11(23):4723–4730. https://doi.org/10.1039/c5sm00230c
38. Shergold OA, Fleck NA (2005) Experimental Investigation Into the Deep Penetration of Soft Solids by Sharp and Blunt Punches, With Application to the Piercing of Skin. Journal of Biomechanical Engineering 127(5):838. https://doi.org/10.1115/1.1992528

39. Jiang S, Li P, Yu Y, Liu J, Yang Z (2014) Experimental study of needle-tissue interaction forces: Effect of needle geometries, insertion methods and tissue characteristics. Journal of Biomechanics 47(13):3344–3353. https://doi.org/10.1016/j.jbiomech.2014.08.007
40. Clough JM, Creton C, Craig SL, Sijbesma RP (2016) Covalent Bond Scission in the Mullins Effect of a Filled Elastomer: Real-Time Visualization with Mechanoluminescence. Advanced Functional Materials 26(48):9063–9074. https://doi.org/10.1002/adfm.201602490
41. Lake GJ, Thomas AG (1967) The Strength of Highly Elastic Materials. Proceedings of the Royal Society A: Mathematical, Physical and Engineering Sciences 300(1460):108–119. https://doi.org/10.1098/rspa.1967.0160
42. De D, Gent AN (1996) Tear strength of carbon-black-filled compounds. Rubber Chemistry and Technology https://doi.org/10.5254/1.3538406
43. Bhowmick AK, Neogi C, Basu SP (1990) Threshold tear strength of carbon black filled rubber vulcanizates. Journal of Applied Polymer Science 41(5-6):917–928. https://doi.org/10.1002/app.1990.070410504
44. Lake GJ, Lindley PB (1965) Mechanical Fatigue Limit for Rubber. Rubber Chemistry and Technology 39(4):348–364. https://doi.org/10.5254/1.3544847
45. Gent AN (1996) A New Constitutive Relation for Rubber. Rubber Chemistry and Technology 69(1):59–61. https://doi.org/10.5254/1.3538357. 0002163820

Supplementary Information

Y-Shaped Cutting for the Systematic Characterization of Cutting and Tearing

B. Zhang · C.-S. Shiang · S.J. Yang · S.B. Hutchens[1]

Blade Radius

Blade radii are gathered from cleaved, or machine-cut blades using scanning electron microscopy (SEM). Figure S1 shows the images taken from each of the blade types used for cutting.

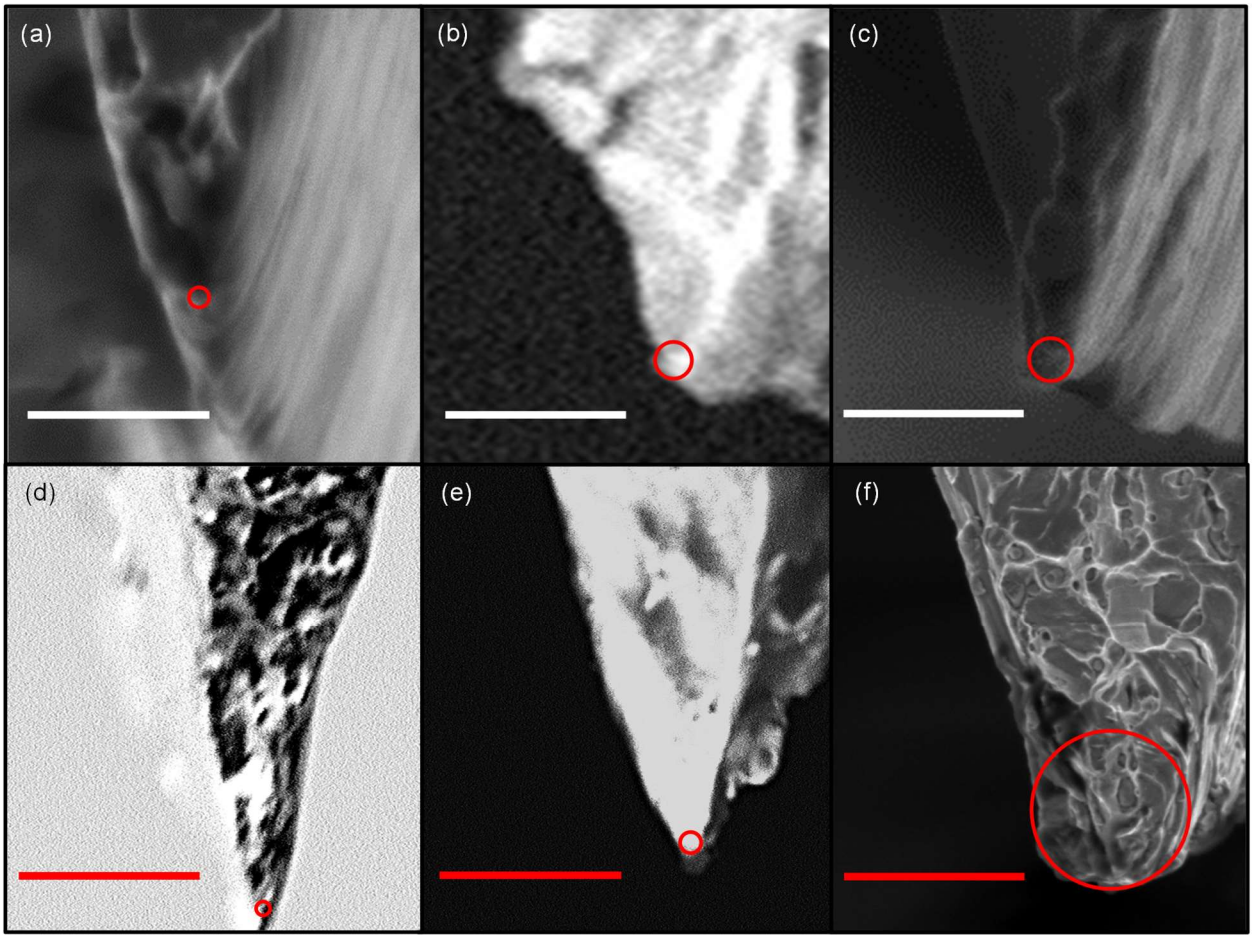

Fig. S1 SEM images of the tips of six selected razor blades. The blade tip radius is measured by fitting the largest possible inscribed circle to the profile of the blade tip cross-section. The selected razor blades and their measured radii are: (a) feather razor blade, $r \approx 37.0$ nm; (a) shaving razor blade, $r \approx 86.0$ nm; (c) utility razor blade, $r \approx 127.0$ nm; (d) blunted utility razor blade #4, $r \approx 198.1$ nm; (e) trapezoid razor blade, $r \approx 245.6$ nm; (f) blunted utility razor blade #2, $r \approx 2080.0$ nm. Scale bars: white, 1 μm; red, 5 μm

[1] Corresponding author (hutchs@illinois.edu)

Tearing

Tearing energy was obtained using a pure shear tearing geometry as detailed in Figure S2. A rectangular test sample (2 mm t × 60 mm w × 10 mm h, Fig. S2(c)) is stretched uniaxially at a constant quasi-static strain rate (~ 0.002 1/s) to obtain the load-displacement response with and without an edge notch (length ~ 10 mm). The critical displacement at the onset of spontaneous crack propagation, u_c, is used to calculate the tearing energy via the following equation [46]:

$$G_{c,\text{tear}} = \frac{U_w(u_c)}{wt} \tag{S1}$$

where U_w is the work done by load F in the un-notched sample. $U_w(u_c)$ is determined by integrating the force displacement curve from zero displacement to the displacement at crack propagation, u_c (Fig. S2(b)). Samples are imaged during testing in order to determine the onset of crack propagation (Fig. S2 (a) & (d)).

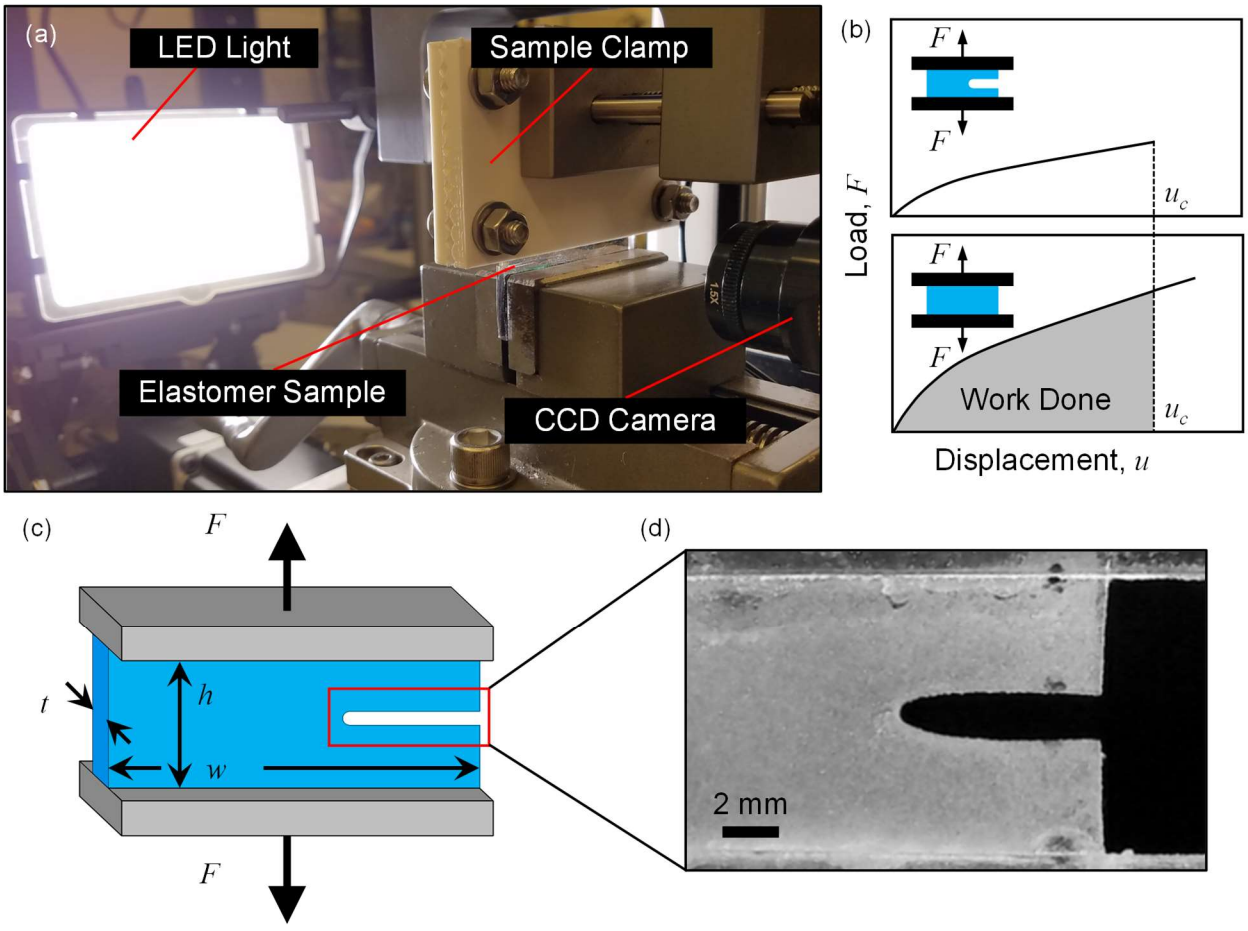

Fig. S2 The apparatus (a) and schematics (b and c) of the pure-shear tearing test. A notched sample (c) is used to determine the critical displacement, u_c, at the onset of crack propagation (b, reproduced from [47] with permission). The tearing energy is determined using Eqn. (S1), which requires integration of the force-displacement curve of the un-notched sample ((b), bottom) [46]. (d) An optical image of the crack at the onset of propagation.

Cutting Rate

Figure S3 presents rate dependent cutting results obtained from constant rate tests performed on 10:1 Sylgard 184. The results validate the relative rate independence of the cutting response in this highly elastic material. The relative change in $G_{c,\text{cut}}$ across the order of magnitude variation in cutting speed is ~ 6.8% (compared to $G_{c,\text{cut}}$ at 10 mm/min), while changes due to leg angle and blade radius (Figure 5(a) and 7(a)) are an order of magnitude larger, ~ 53% and ~ 88%, respectively.

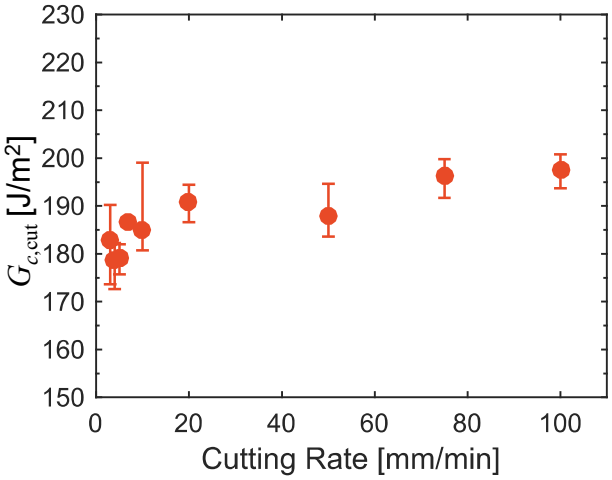

Fig. S3 The cutting energy of 10:1 Sylgard 184 measured at cutting rates ranging from 3 to 100 mm/min. Error bars represent maximum and minimum cutting energy values from at least three samples.

The Vanishing Loading-History Effect in Speed Sweep Tests

Figure S4 presents the results of speed sweep tests obtained through either acceleration (0-15 mm/min, unfilled symbols) or deceleration (15-0 mm/min, filled symbols) approach for different material systems and leg angles. Close agreement between the acceleration and deceleration curves (Fig. S4) demonstrates that loading-history does not affect the test results.

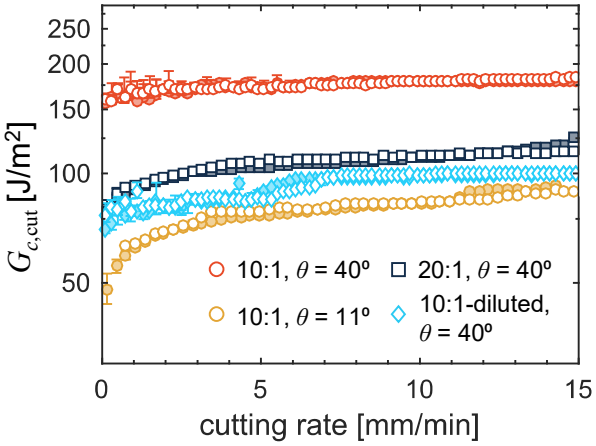

Fig. S4 Speed sweep test results in three material systems at different leg angles. Cutting rate is increased (unfilled symbols) or decreased (filled symbols) at a rate of 2.16 mm/min^2.

Determination of Strain Distribution Using Digital Image Correlation

The strain distribution approaching the crack tip of a 'Y-shaped' sample (10:1) is determined using two-dimensional digital image correlation (2D DIC). The speckle pattern is applied on the front surface of the sample with matte black spray paint. The size of a speckle is ~ 100 μm. Image capture is illustrated in Figure S5. A charge-coupled device (CCD) camera (PixeLINK® ½" CMOS 1.3 MP) is mounted in front of the sample at its focal distance with 1x magnification. The sample is backlit with diffuse white light. Images gathered at a frame rate of 2 Hz are synchronized with the cutting process. The strain distribution is calculated via 2D DIC MATLAB software (Ncorr, Georgia Institute of Technology, v1.2.1)[2]. A Eulerian coordinate system is selected to mitigate the effect of sample translation during cutting. The strain distribution is extracted along the centerline of the sample approaching the crack tip.

The measured strain distribution, ε_{11} appears to evolve with time as cutting progresses (Figure S6(b), white circles). We attribute this apparent evolution to the effect of residual strains from taking on the Y-shape, bringing the blade into contact, and release of any elastic loading from initial indentation. The strain distribution eventually stabilizes and maintains a constant magnitude and shape. (Fig. S6(b), the blue circles represent the last ~ 20% of the data gathered from the region of small, uniform reference area.) From the stabilized strain distribution, the instantaneous strain rate, $\dot{\varepsilon}_{11}$, at each point ahead of the tip is determined by

$$\dot{\varepsilon}_{11}(d) = v\frac{\partial \varepsilon_{11}}{\partial d} \tag{S2}$$

where v is the cutting speed and d is the distance from the crack tip. The distribution of strain, ε_{22} is not included in Fig. S6 because it is one order of magnitude smaller than ε_{11} along the same path.

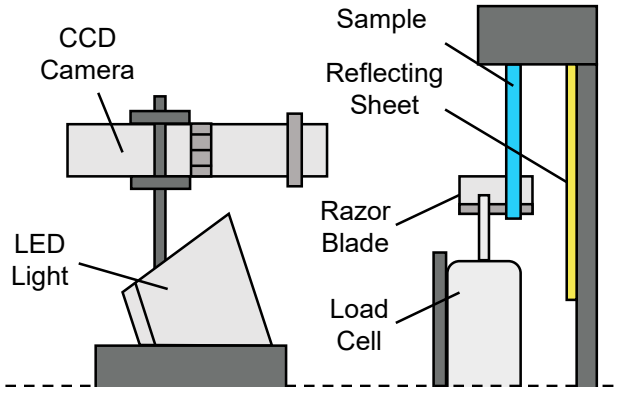

Fig. S5 Schematic of the DIC image capture setup

[2] Link: http://www.ncorr.com/index.php/downloads. Date of download: 11/28/2016

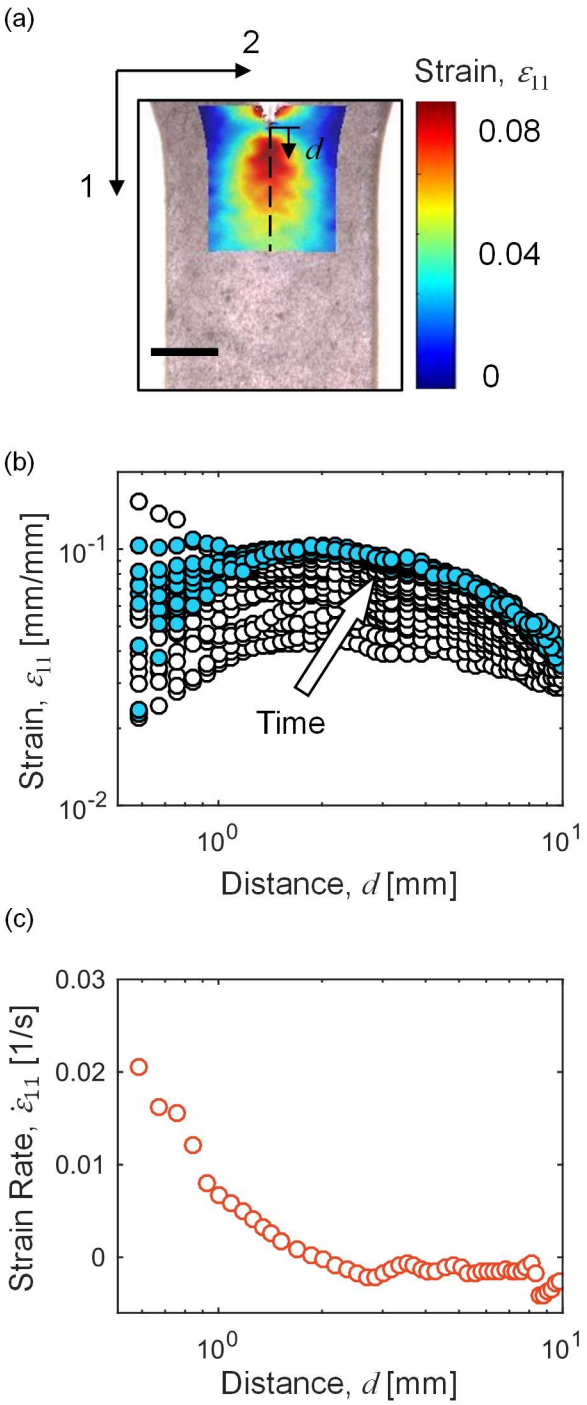

Fig. S6 DIC results. The DIC strain map (a) shows the overall strain distribution near the crack tip. Scale bar: 5mm. Along the centerline (dashed line) the strain distribution (b) and strain rate distribution (c) are plotted as a function of the distance from the crack tip, d. (c) The stabilized strain distribution is used to evaluate the local strain rate according to Eqn. (S2). We truncate both the strain and strain rate at $d < 0.5$ mm from the crack tip due to the increase of scatter and the lack of correlation beyond this distance.

An Exact Derivation of the Cutting Energy

The form for the cutting energy of a Y-shaped sample published by Lake and Yeoh [14] utilizes an unusual approximation that combines cross-leg first order energy terms with a zeroth order approximation for the leg stretch ($\lambda_A \approx \lambda_B \approx 1$). Here we derive the full expression, without these approximations and show that in most practical experimental cases, the difference between the full expression and Lake and Yeoh's simplified one are inconsequential. Exploring these fracture energy equations further, we demonstrate the separability of energy into essentially independently-tunable cutting and tearing terms.

Derivation of 'Y-shaped' Cutting Energy without Approximation

Similar to the energetic arguments of Lake and Yeoh [14], we derive a full analytical expression for the cutting energy. The cutting energy is determined from energy arguments similar to those used to extract the strain energy release rate.

$$G_c = \frac{\partial\left(U_w - U_{el}\right)}{\partial A} = \lim_{\delta A \to 0} \frac{\delta U_w - \delta U_{el}}{\delta A}, \tag{S3}$$

where U_w is the external work done on the sample, U_{el} represents the stored elastic energy, and A is the fracture surface area. In this derivation, we do not use the inconsistent assumption of $\lambda_A \approx \lambda_B \approx 1$. All deformations are assumed to be linear elastic. The work done on the legs A and leg B (Fig. 1(b)) by constant forces f_A and f_B, respectively, is due to displacement of the legs, $\delta\ell_A$ or $\delta\ell_B$ as a result of the propagation of the crack by an infinitesimal length, δc. Because the loads on the legs are constant and uniform deformation is assumed within each, the stretch ratio in each leg, $\lambda = \ell / \ell_0$, is the same before and after the cut propagates. Here ℓ_0 is the original length. It follows that

$$\delta\ell_A = \lambda_A \delta c \text{ and } \delta\ell_B = \lambda_B \delta c. \tag{S4}$$

Note that the blade contact is taken as the fixed reference point. Thus, the work done on the legs is given by

$$\delta U_w = 2 f_A \delta\ell_A - f_B \delta\ell_B = \left(2\lambda_A f_A - \lambda_B f_B\right)\delta c, \tag{S5}$$

where the negative second term is due to the opposite actions of $\delta\ell_B$ and f_B.

Similarly, the strain energy change in the sample due to the crack propagation is given by the superposition of the two regions

$$\delta U_{el} = 2\delta U_A + \delta U_B = 2W_A A_A \delta\ell_A - W_B A_B \delta\ell_B, \tag{S6}$$

with the changes in strain energy of the regions A and B (δU_A and δU_B, respectively) being characterized using their respective strain energy densities, W_A and W_B. The change in volume of that region is the product of the deformed cross-sectional areas, A_A and A_B, and the crack propagation distance, δc. Applying incompressibility, the deformed cross-sectional areas may be expressed in terms of the applied stretch as:

$$A_A = \frac{wt}{2\lambda_A} \text{ and } A_B = \frac{wt}{\lambda_B}, \tag{S7}$$

where w and t are the undeformed thickness and uncut sample width (Fig. 1(b)). Substituting Eqns. (S4) and (S7) into (S6) yields an expression for δU_{el} in terms of the strain energy density,

$$\delta U_{el} = \left(W_A - W_B\right) wt\delta c. \tag{S8}$$

Invoking linear elasticity, we determine the strain energy density for a region, $W = 1/2\, E\left(\lambda - 1\right)^2$, with E being the Young's modulus. Expressing the Young's modulus in terms of the applied loads and stretch values ($E = f/\left[A\left(\lambda - 1\right)\right]$) and applying Eqn. (S7) yields

$$W_A = \frac{f_A}{wt}\lambda_A\left(\lambda_A - 1\right) \text{ and } W_B = \frac{1}{2}\frac{f_B}{wt}\lambda_B\left(\lambda_B - 1\right), \tag{S9}$$

which when substituted into Eqn. (S8) yields an expression for the strain energy change in terms of experimentally measurable variables.

$$\delta U_{el} = \frac{1}{2}\left[2f_A\lambda_A\left(\lambda_A - 1\right) - f_B\lambda_B\left(\lambda_B - 1\right)\right]\delta c. \tag{S10}$$

Static equilibrium relates the force applied to leg B to the loads applied to legs A and the measured cutting force, f_{cut}.

$$f_B = 2f_A\cos\theta - f_{\text{cut}} \tag{S11}$$

Substituting Eqns. (S5) and (S10) into Eqn. (S3), using Eqn. (S11), and applying the relation $\delta A = t\delta c$ results in the full expression for the strain energy release rate for cutting,

$$G_{c,\text{cut}} = \underbrace{\frac{f_A}{t}\left[\lambda_A\left(3 - \lambda_A\right) - \lambda_B\left(3 - \lambda_B\right)\cos\theta\right]}_{\text{Tearing, } T} + \underbrace{\frac{f_{\text{cut}}\lambda_B\left(3 - \lambda_B\right)}{2t}}_{\text{Cutting, } C}. \tag{S12}$$

Lake and Yeoh [14] simplified this expression by approximating Eqn. (S10) as $1/2\left(2f_A + f_B\right)\left(\lambda_A - \lambda_B\right)\delta c$, essentially approximating the stretches λ_A and λ_B to the zero order, such that $\lambda_A \approx \lambda_B \approx 1$, which yields the simpler, but less exact form,

$$G_{c,\text{cut}} = \underbrace{\frac{2f_A\overline{\lambda}}{t}\left(1 - \cos\theta\right)}_{\text{Tearing, } T} + \underbrace{\frac{f_{\text{cut}}\overline{\lambda}}{t}}_{\text{Cutting, } C}, \tag{S13}$$

where $\overline{\lambda} = \left(\lambda_A + \lambda_B\right)/2$. Note that in both expressions (Eqns. (S12) and (S13)), we denote the first and second terms as "Tearing" and "Cutting", respectively [14]. The tearing term, T, is dominated by the applied load on legs A and the tearing angle, θ. The cutting force determines the contribution from the cutting term, C. λ_B and $\overline{\lambda}$ are found in both terms and vary with the applied *tearing* load on legs A, f_A; the tear inducing angle between them, θ; and the *cutting* force, f_{cut}. Although λ_B and $\overline{\lambda}$ introduce these combined cutting/tearing contributions into both terms, satisfying linear elasticity suggests that both differ from one by 10% or less. Thus, these multi-

contribution-containing terms are constrained to change very little with changes in the applied load, f_A, or leg angle, θ ($\lambda_A(3-\lambda_A)\approx 2$, $\lambda_B(3-\lambda_B)\approx 2$ and $\bar{\lambda}\approx 1$). Thus, the Y-shaped geometry effectively separates the cutting energy contribution from the tearing energy contribution. As we will show in the next subsection, the discrepancy between Eqns. (S12) and (S13) is small (less than experimental resolution) for low applied stretch values. One could derive Eqn. (S12) for a hyperelastic solid, however our experience thus far is that loads large enough to induce nonlinearity (i.e., $\lambda_A > 1.1$) often produce spontaneous tearing in the system, making steady-state cutting irrelevant.

Applicability of the Approximate Cutting Energy Expression

In this section, we quantify the difference between Eqns. (S12) and (S13). We find no experimentally measurable difference in the total G_c, but a noticeable effect between the two expressions when the energy is separated into cutting and tearing components. The approximate expression underestimates the tearing component (Fig. S7(b)) while overestimating the cutting component (Fig. S7(c)) for a range of applied loads, f_A such that λ_A remains within a linear elastic regime ($\lambda_A < 1.1$). (Note that in our experiments, $0.02 \lesssim f_A/(wtE) \lesssim 0.03$, so that $\lambda_A \lesssim 1.06$.) These findings derive from re-expressing Eqns. (S12) and (S13) as functions of the dimensionless quantities $f_A/(wtE)$, f_{cut}/f_A, and θ.

To reformulate these expressions one first recognizes that λ_A and λ_B are theoretically related to one another, both being functions of f_A. λ_B is also a function of f_{cut}/f_A and θ. Drawing upon linear elasticity, incompressibility, and the constraint of static equilibrium, these stretches are determined,

$$\lambda_A = \left(1 - 2\frac{f_A}{wtE}\right)^{-1} \text{ and } \lambda_B = \left[\frac{f_A}{wtE}\left(f_{\text{cut}}/f_A - 2\cos\theta\right) + 1\right]^{-1}, \tag{S14}$$

such that

$$\frac{G_{c,\text{cut}}}{wE} = \frac{G_{c,\text{cut}}}{wE}\left(\frac{f_A}{wtE},\ f_{\text{cut}}/f_A, \theta\right). \tag{S15}$$

Fig. S7(a) reports the percent difference between the two $G_{c,\text{cut}}/(wE)$ determined in this way for the smallest and largest θ that we tested ($11°$ and $40°$). Experimentally, we observe that f_{cut}/f_A falls within the range of 0.07 to 1.4 for our silicone materials, the former motivating the lower value of the f_{cut}/f_A isolines in Fig. S7; there is also a practical upper limit at $f_{\text{cut}}/f_A = 2\cos\theta$ corresponding to a transition to loss of tensile load in leg B.

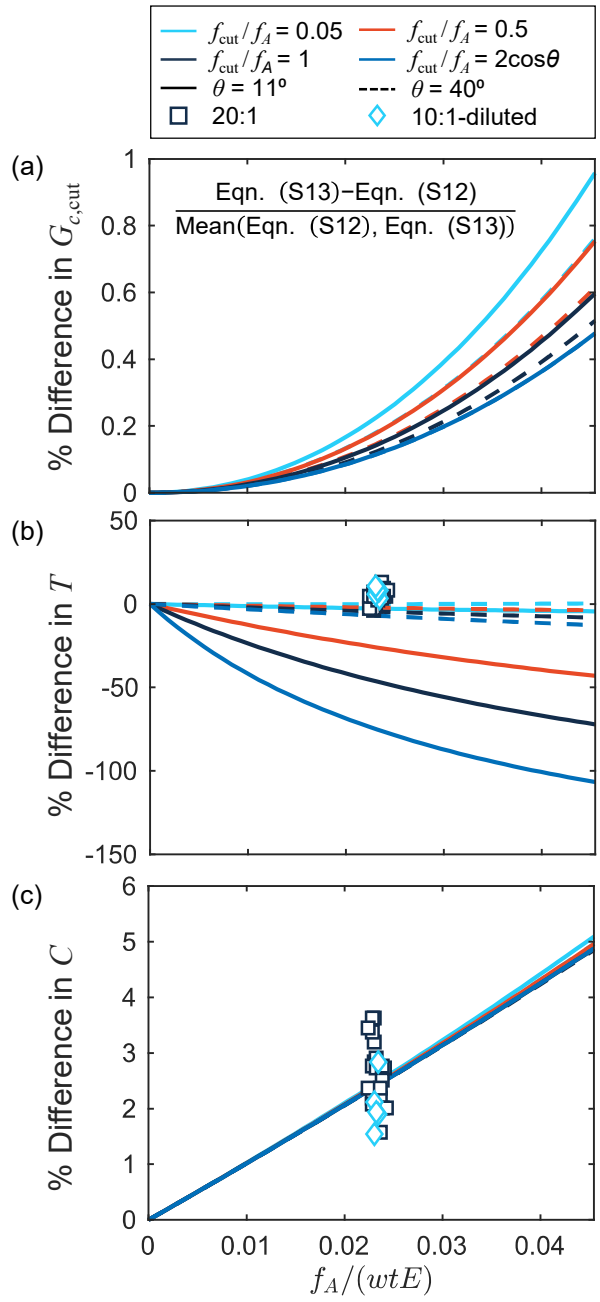

Fig. S7 A comparison between the two expressions for $G_{c,\text{cut}}$, Eqns. (S12) and (S13), as a function of stiffness-normalized pre-load, $f_A/(wtE)$. Percent difference is calculated according to the equation shown. Curves for selected values of the normalized cutting force, f_{cut}/f_A, are denoted by color: 0.05 (cyan), 0.5 (orange), 1 (navy), and $2\cos\theta$ (blue). Solid and dashed lines denote calculations for $\theta = 11°$ and $\theta = 40°$, respectively. (a) The percent difference in cutting energy, $G_{c,\text{cut}}$, increases with increasing pre-load. (b) The percent difference in tearing contribution, T, varies most strongly with θ. (c) The percent difference in cutting contribution, C, is largely independent of both f_{cut}/f_A, and θ. Experimental data are plotted for comparison ($\theta = 40°$): 10:1-diluted (cyan diamonds), 20:1 (navy squares).

In all cases, the difference between expressions (S12) and (S13) increases with increasing load or deformation of the legs A. The theoretical discrepancy between them as a function of either θ or f_{cut}/f_A is primarily due to variations in the tearing contribution, which exhibits a dependence on θ and f_{cut}/f_A (Fig. S7(b)) that the cutting contribution depends upon only weakly (Fig. S7(c)). This latter point further justifies the separability of cutting and tearing contributions. We plot discrepancies in the calculation of C and T for sample experimental data at $f_{\text{cut}}/f_A \approx 0.5$ for comparison ($\theta = 40°$: 10:1-diluted, cyan diamonds; 20:1, navy squares). Good agreement exists for percent differences in calculated C values, but no observable trend occurs for the variation in calculated T values. The estimated tearing energy difference calculated from experimental data is higher than predicted. This discrepancy is likely due to poor experimental precision in determination of the stretch in the legs ($\lambda = \lambda \pm 0.02$). This issue is being corrected in future test procedures.

The deviation of the difference tearing energy results in a larger difference between the calculated $G_{c,\text{cut}}$ values than predicted in Fig. S7(a). However, the discrepancy between the two expressions for $G_{c,\text{cut}}$ is less than the experimental scatter. For simplicity therefore, we use Lake and Yeoh's expression.

Comparison of Numerical Values from Cutting and Pure Shear Testing

Table S1 Plateau $G_{c,\text{cut}}$ and pure shear $G_{c,\text{tear}}$ values from Figure 6(a)

Material System	10:1	20:1	10:1-diluted	10:1 ($\theta = 31°$)
Plateau $G_{c,\text{cut}}$ (J/m²)	175.5	97.5	93.6	128.8
$G_{c,\text{tear}}$ (J/m²)*	165.9 ± 9.0	60.7 ± 7.4	43.0 ± 2.7	–
$G_{c,\text{tear}} / G_{c,\text{cut}}$	0.95	0.62	0.46	–

* The ranges reflect standard deviations across three samples

Calculation of the Elasto-Cohesive Length

Table S2 Elastocohesive length scale from pure shear measurements

Material	**G_c (from pure shear) [J/m²]**	**E (from Gent fit) [MPa]**	**$\rho^* \sim G_c / E$ [μm]**
10:1	166 ± 9	0.942	176
10:1-diluted	43 ± 3	0.396	109
20:1	61 ± 7	0.305	200

Table S3 Elastocohesive length scale using applied tearing component, T, from 40° radius dependent data

Material	**T (cutting test vs. r) [J/m²]**	**E (from Gent fit) [MPa]**	**$\rho^* \sim T / E$ [μm]**
10:1	153	0.942	162
10:1-diluted	69	0.396	174
20:1	54	0.305	177

Relevant Material Length Scales

Nanoparticle sizes and concentrations and the polymer network set several characteristic length scales for the Sylgard 184-based materials.

Silica Particle Content

Clough et al. estimate the nanoparticle content of 10:1 Sylgard 184 at a volume fraction of 0.16 with particles themselves around 10 nm in size arranged in ~100 nm aggregates [40]. Using this volume fraction as a reference point and assuming that nanoparticles are found within the pre-polymer and not the crosslinking component of Sylgard 184, the volume fraction may be estimated. The former yields a pre-polymer mass fraction, $f' = 0.454$. The volume fraction of the 20:1 and 10:1-diluted materials, ϕ, may be estimated from $\phi = f \rho_{\text{Sylgard}} / \rho_{\text{silica}}$, where f is the mass fraction given by:

$$f_{20:1} = \frac{f'}{1+\frac{1}{20}} \text{ and } f_{10:1\text{d}} = \frac{f'(1-0.3)}{1+\frac{1}{10}} \tag{S16}$$

The above expressions arise from the ratio of nanoparticle mass to total mass, with 1/20 coming from the 20:1 mixing ratio and 1/10 and 0.3 coming from the mixing ratio and silicone oil mass fraction, respectively. Using $\rho_{\text{Sylgard}} = 1027\ \text{kg/m}^3$ and $\rho_{\text{silica}} = 2650\ \text{kg/m}^3$, the volume fraction of 20:1 and 10:1-diluted are estimated to be 0.17 and 0.11, respectively. Interparticle spacing is estimated using the following expression [48]:

$$\text{IPS} = 2r\left[\left(\frac{\phi_{\max}}{\phi}\right)^{1/3} - 1\right] \tag{S17}$$

where r is the particle (in this case aggregate) radius, 50 nm, and $\phi_{\max}$ is the maximum volume fraction taken to be equal to loose random packing, 0.56. The resulting interparticle spacing values for 10:1, 20:1, and 10:1-diluted samples are 52 nm, 49 nm, and 72 nm, respectively.

Approximate Mesh Size

The maximum mesh size for a polymer network can be approximated using the entanglement characteristics of the chains. The entanglement length, N_e, for PDMS is 32; The Kuhn length, b, is 13Å [49]. The root mean square end-to-end distance for an ideal chain scales as $bN^{1/2}$. It follows that the maximum mesh size for a PDMS network is around 7.4 nm.

Swell Testing

Two cylindrical samples (20 mm diameter × 10 mm height) are prepared for each of the three gels (10:1, 10:1-diluted and 20:1) using Teflon molds. The samples are submerged in HPLC grade toluene (99.9%, Sigma-Aldrich, 34866) at room temperature for 6 days before reaching an equilibrium state. The weight and volume of a sample are measured every 24 hours immediately after removing the sample and drying excessive solvent. The equilibrium weight and volume are recorded at final values (change between two measurements < 1%) for 10:1 and 20:1 samples and maxima for 10:1-diluted samples. (A post-equilibrium weight drop exists for 10:1-diluted samples presumably due to dissolution of linear PDMS chains in toluene.)

The weight swelling ratio, Q_W, is calculated using the equation,

$$Q_W = \frac{W_s - W_d}{W_d}, \tag{S18}$$

where W_s is the equilibrium weight after swelling and W_d represent the initial dry weight of the elastomer. The volumetric swelling ratio, Q_V, is obtained through the expression,

$$Q_V = \frac{V_s}{V_d}, \tag{S19}$$

where V_d denotes the initial dry volume of the elastomer and V_s represents the volume of the swollen gel. The calculated swelling ratios for 10:1, 10:1-diluted and 20:1 gels are listed in Table S4, averaged between two samples.

Table S4 Swelling Ratios of Sylgard 184 networks

Material	10:1	10:1-diluted	20:1
Q_W	1.3	1.7	2.7
Q_V	2.5	3.0	4.3

References

14. Lake GJ, Yeoh OH (1978) Measurement of rubber cutting resistance in the absence of friction. International Journal of Fracture 14(5):509–526. doi: 10.1007/BF01390472
40. Clough JM, Creton C, Craig SL, Sijbesma RP (2016) Covalent Bond Scission in the Mullins Effect of a Filled Elastomer: Real-Time Visualization with Mechanoluminescence. Advanced Functional Materials 26(48):9063–9074. doi: 10.1002/adfm.201602490
46. Sun J-Y, Zhao X, Illeperuma WRK, et al (2012) Highly stretchable and tough hydrogels. Nature 489:133–136. doi: 10.1038/nature11409
47. Zhang B (2016) Fabrication and Mechanical Characterization of Liquid-in-Solid Elastomeric Soft Composites. University of Illinois at Urbana-Champaign
48. Hao T, Riman RE (2006) Calculation of interparticle spacing in colloidal systems. Journal of Colloid and Interface Science 297(1):374-377. doi: 10.1016/j.jcis.2004.10.014
49. Rubinstien M, Colby RH (2003) Polymer Physics. Oxford University Press.